HHS Public Access

Author manuscript

Cell Stem Cell. Author manuscript; available in PMC 2020 November 07.

Published in final edited form as:

Cell Stem Cell. 2019 November 07; 25(5): 682–696.e8. doi:10.1016/j.stem.2019.08.003.

Cohesin members Stag1 and Stag2 display distinct roles in chromatin accessibility and topological control of HSC self-renewal and differentiation

Aaron D. Viny[1,2,3], **Robert L. Bowman**[1,3], **Yu Liu**[4], **Vincent-Philippe Lavallée**[5], **Shira E. Eisman**[1,3], **Wenbin Xiao**[1,6], **Benjamin H. Durham**[1,6], **Anastasia Navitski**[1,3], **Jane Park**[3], **Stephanie Braunstein**[1,3], **Besmira Alija**[1,3], **Abdul Karzai**[1,3], **Isabelle S. Csete**[1,3], **Matthew Witkin**[3], **Elham Azizi**[5], **Timour Baslan**[7], **Christopher J. Ott**[8], **Dana Pe'er**[5], **Job Dekker**[4,9], **Richard Koche**[3], **Ross L. Levine**[1,2,3,*]

[1]Human Oncology and Pathogenesis Program and Center for Hematologic Malignancies, Memorial Sloan Kettering Cancer Center, New York, NY, 10065 USA

[2]Department of Medicine, Leukemia Service, Memorial Sloan Kettering Cancer Center, New York, NY, 10065 USA

[3]Center for Epigenetics Research, Memorial Sloan Kettering Cancer Center, New York, NY, USA

[4]Program in Systems Biology, Department of Biochemistry and Molecular Pharmacology, University of Massachusetts Medical School, Worcester, Massachusetts 01605, USA

[5]Center for Computational and Systems Biology, Memorial Sloan Kettering Cancer Center, New York, NY, 10065 USA

[6]Department of Pathology, Memorial Sloan Kettering Cancer Center, New York, NY, USA

[7]Cancer Biology and Genetics Program, Memorial Sloan Kettering Cancer Center, New York, NY, 10065 USA

[8]Massachusetts General Hospital Cancer Center, Harvard Medical School, Boston, MA, USA

[9]Howard Hughes Medical Institute, 4000 Jones Bridge Road, Chevy Chase, MD, 20815 USA

Summary

Transcriptional regulators, including the cohesin complex member STAG2, are recurrently mutated in cancer. The role of STAG2 in gene regulation, hematopoiesis, and tumor suppression

[*]Correspondence to: Ross L. Levine, MD, Human Oncology and Pathogenesis Program, Leukemia Service, Department of Medicine, Center for Epigenetics Research, Center for Hematologic Malignancies, Memorial Sloan Kettering Cancer Center, 1275 York Ave, Box 20, New York, NY 10065, leviner@mskcc.org.
Lead Contact: Ross L. Levine, MD

Author Contributions: Conceptualization, ADV, RLB, RLL Methodology, ADV, RLB, YL, VL, WX, TB, CJO, DP, JD, RK, RLL Investigation, ADV, RLB, YL, WX, BHD, SEE, AN, JP, SB, BA, AK, ISC, MW, TB, CJO, RK Writing – Original Draft, ADV, RLB Writing – Review & Editing, ADV, RLB, YL, VP, SEE, WX, BHD, AN, MW, TB, CJO, JD, RK, RLL Funding Acquisition, RLL Resources, JD, RLL Supervision, RLL

remains unresolved. We show Stag2 deletion in hematopoietic 5 stem/progenitor cells (HSPC) results in altered hematopoietic function, increased self-renewal, and impaired differentiation. ChIP-sequencing revealed that while Stag2 and Stag1 bind a shared set of genomic loci, a component of Stag2 binding sites are unoccupied by Stag1 even in Stag2-deficient HSPCs. While concurrent loss of Stag2 and Stag1 abrogated hematopoiesis, Stag2 loss alone decreased chromatin accessibility and transcription of lineage-specification genes, including Ebf1 and Pax5, leading to increased self-renewal and reduced HSPC commitment to the B-cell lineage. Our data illustrate a role for Stag2 in transformation and transcriptional dysregulation distinct from its shared role with Stag1 in chromosomal segregation.

eTOC Blurb

In murine hematopoietic Stag2 deletion, Stag1 rescues topologically associated domains in the absence of Stag2 but cannot restore chromatin architecture required for hematopoietic lineage commitment. PU.1 target genes lose accessibility and expression. Induced target gene expression but not PU.1 overexpression is sufficient to restore differentiation in the altered chromatin state.

Graphical Abstract

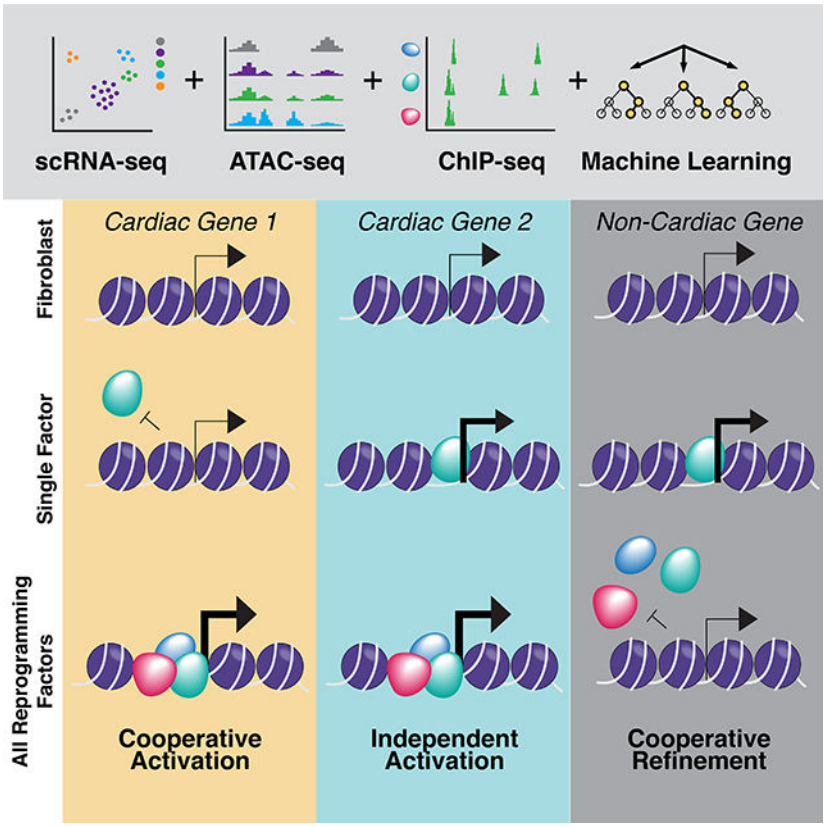

Introduction

Cell-type specific transcriptional programs are regulated in part by the activity of tissue-specific transcription factors and enhancer elements within structurally defined topologically

associating domains (TADs) (Dixon et al., 2012; Nora et al., 2012; Rao et al., 2017). The genes which contribute to transcriptional regulation, including members of the cohesin complex, are frequently mutated in human cancers, including leukemias (Bailey et al., 2014; Balbas-Martinez et al., 2013; Cancer Genome Atlas Research et al., 2013; Kon et al., 2013; Solomon et al., 2011; Thota et al., 2014). Cohesin is a tripartite ring comprised of three structural proteins SMC1A, SMC3, and RAD21; this core complex binds to either STAG1 or STAG2. *STAG2,* which is X-linked, is the most commonly mutated cohesin complex member in human cancer, with recurrent nonsense, frameshift, and missense mutations in Ewing's Sarcoma (40–60%)(Solomon et al., 2011), bladder cancer (20–35%)(Bailey et al., 2014; Balbas-Martinez et al., 2013), glioblastoma (4–5%)(Bailey et al., 2014), myelodysplastic syndrome (MDS; 5–20%)(Kon et al., 2013; Thota et al., 2014), and acute myeloid leukemia (AML; 2–12%)(Cancer Genome Atlas Research et al., 2013; Kon et al., 2013; Thota et al., 2014). This is in contrast to SMC1A, SMC3, and RAD21, which are more commonly mutated in myeloid malignancies than in the broader spectrum of human cancers. The cohesin complex is essential in pleiotropic cellular and gene regulatory functions, including chromosome segregation (Losada et al., 1998; Toth et al., 1999) and in the formation of DNA loops (Rao et al., 2014; Rao et al., 2017; Schwarzer et al., 2017; Seitan et al., 2013) which regulate gene expression (Cuartero et al., 2018; Kagey et al., 2010; Seitan et al., 2013). However, the high mutational frequency and unique mutational spectrum of *STAG2* in human cancers (Bailey et al., 2014; Kon et al., 2013; Thota et al., 2014) suggests a distinct role for *STAG2* in homeostasis and tumor suppression (Mazumdar et al., 2015; Mullenders et al., 2015) which has not been delineated.

Results

Loss of Stag2 alters hematopoietic stem cell function

In order to elucidate the role of *Stag1* and *Stag2* in hematopoietic function/transformation, we generated *Stag1* and *Stag2* conditional knockout alleles. We induced somatic deletion of *Stag1* or *Stag2* in hematopoietic cells through *Mx1*-Cre mediated excision (Figure S1A–H). Following polyinosinic:polycytadinic (PIPC)-mediated deletion, *Mx1*-cre *Stag2* $^{-/-}$ mice compared to cre-negative *Stag2*$^{fl/fl}$ (referred henceforth as KO and WT respectively) manifested an increase in hematopoietic stem cells (HSC), including a significant increase (2.2-fold; $p<0.01$) in the proportion of LSK (Lineage^{-}Sca1^{+}cKit^{+}) cells (Figure 1A). *Stag2* loss, but not Stag1 loss, induced an expansion of multipotent progenitors (MPP: LSK $^{+}$Cd150^{-}Cd48^{+}Cd127^{-}; $p<0.04$), short term HSCs (ST-HSC: LSK^{+}Cd150^{-}Cd48^{-}; $p<0.001$), and long-term HSCs (LT-HSC: LSK^{+}Cd150^{+}Cd48^{-}; $p<0.02$) (Figure S1I). We also observed a significant increase in granulocyte macrophage progenitors (GMP: Lineage^{-}cKit $^{+}$Sca1^{-}Cd34^{+}Fcγ^{+}; $p<0.001$; Figure S1J–K) in the *Stag2*-deficient hematopoietic compartment.

We next investigated the role of Stag2 and Stag1 in hematopoietic self-renewal. *Stag2*-deficient hematopoietic cells displayed increased serial replating capacity in methylcellulose culture assays (≥7 platings), whereas WT and *Stag1* KO cells were not able to form colonies beyond 3 platings (Figure 1B). We next performed competitive transplantation assays to assess the impact of Stag2/Stag1 loss on self-renewal *in vivo*. We observed reduced *Stag2*-

deficient derived chimerism in the peripheral blood of mice reconstituted with Stag2 KO and WT competitor cells ($p<0.001$; Figure S1L–N). However, within the bone marrow of transplant recipient mice, we found a significant increase in *Stag2* KO derived chimerism, which was most significant in the LSK compartment ($p<0.001$) including in LT-HSCs ($p<0.001$; Figure 1C) but not in lineage positive cells ($p\leq0.37$). *Stag1* loss did not impact *in vivo* self-renewal or differentiation output (Figure 1D; S1O–Q). These data suggest that *Stag2* loss induces both an increase in self-renewal and reduced differentiation capacity in HSCs, which are critical features of hematopoietic transformation.

To determine if Stag2 loss was associated with the expansion of hematopoietic cells with clonal cytogenetic alterations, we performed karyotype analysis in *Stag2* and *Stag1* WT and KO bone marrow cells. Chromosomal aberrations by metaphase karyotyping were not detected in either *Stag2*- or *Stag1*-deficient hematopoietic cells (n=7; Figure S2A–B). We did observe an increase in the proportion of cells with premature sister chromatid separation in *Stag2* KO bone marrow (Figure S2C); however, consistent with metaphase cytogenetics, we did not observe clonal copy number alterations on low-pass whole genome sequencing (Figure S2D–E). This data suggested that the increase in hematopoietic self-renewal induced by *Stag2* loss is not due to genomic instability and resultant clonal evolution.

Stag2 and Stag1 concurrent deletion is synthetic lethal

The observation that *Stag2*-deficient HSCs displayed increased self-renewal is in contrast to the lethality observed with loss of the core cohesin component *Smc3* in hematopoietic cells (Viny et al., 2015). We next sought to evaluate potential compensatory function among the Stag paralogs. We found *Stag1* transcript and protein expression were significantly increased in *Stag2* KO hematopoietic cells ($p<0.05$), whereas *Stag2* expression was not altered in *Stag1* KO hematopoietic cells ($p<0.65$; Figure S2F–I). Analysis of the AML TCGA dataset showed that AML patients with STAG2 mutations expressed higher levels of *STAG1* ($p<0.006$; Figure S2J), suggesting compensatory regulation. We hypothesized that Stag1 and Stag2 may have redundant roles with respect to chromatid segregation. *In vitro* studies have recently nominated STAG1 as a synthetic lethal target in *STAG2* mutant cell lines (Benedetti et al., 2017; van der Lelij et al., 2017); however, this has not been assessed *in vivo*. We generated mice with hematopoietic cells retaining one or zero copies of *Stag1* on the background of a *Stag2* (hemizygous male) KO genotype. $Stag2^{-/y}/Stag1^{+/-}$ mice developed rapid, progressive thrombocytopenia ($p<0.001$) and impaired survival ($p<0.001$) due to bone marrow failure (median survival of 27.7 weeks). Complete loss of *Stag1* and *Stag2* in hematopoietic cells induced rapid lethality (median survival 0.7 weeks; Figure 1E; Figure S2K). *Stag1/Stag2* deficient mice were characterized by pancytopenia and bone marrow aplasia, consistent with redundancy in hematopoietic function and in alignment with the absolute requirement for core cohesin complex members (Viny et al., 2015) (Figure 1F). Similar to mice with bi-allelic deletion of *Smc3*, we observed marked chromosomal alterations on metaphase spreads of the *Stag1/Stag2* deleted bone marrow (Figure S2L). Collectively, these data suggest a role for Stag2 in gene regulation and tumor suppression that is not shared with Stag1, whereas they have a shared, redundant role in chromosomal segregation.

Stag2 alters transcriptional lineage commitment

We hypothesized that *Stag2* loss induced alterations in transcriptional output which dysregulate hematopoietic function and promote transformation. To investigate transcriptional mechanisms regulating self-renewal and differentiation in the context of *Stag2* loss, we performed RNA-sequencing (RNAseq) on *Stag2* KO and WT LSK cells. We identified 186 genes which were significantly downregulated and 42 genes which were significantly upregulated in *Stag2* KO compared to WT cells (Figure S3A). We observed reduced expression of *Ebf1, Vbrep3, Cd19, Bank1*, and *Pax5,* suggesting a loss of B-cell lineage commitment (Herman et al., 2018; Zandi et al., 2008). We observed reduced expression of *Vwf (*Grover et al., 2016*), Hba-a1, Hba-a2, Hbb-b1(*Kingsley et al., 2013*), Fcgr2b (*Ferrari et al., 2007*), Ccr2 (*Reid et al., 1999*), Spib (*Su et al., 1997*), S100a8*, *and S100a9* (Lagasse and Weissman, 1992), genes associated with myeloid/erythroid lineage commitment. Gene set enrichment analysis (GSEA) revealed that Stag2 deficient LSKs showed negative enrichment of genes associated with cell lineage specification (Figure S3B). We further found increased expression of the Hoxb4-target *Hemgn* (Jiang et al., 2010), as well as of *Itgb3* (Umemoto et al., 2006), a Periostin-binding integrin shown to mediate HSC self-renewal. Coupled with downregulation of *Flt3* (Adolfsson et al., 2001) and *Selp* (P-selectin) (Sullivan et al., 2011), these findings indicate an LSK pool that is transcriptionally skewed towards increased self-renewal.

Given the heterogeneity of the LSK compartment, we sought to determine if the transcriptional alterations observed in bulk LSKs were due to a subpopulation wide shift or a result of cell intrinsic differential expression. We performed single cell RNA-seq (scRNAseq) of ~24,000 Lin^- hematopoietic stem/progenitor cells (HSPC) from Stag2 KO (n=3) and WT (n=3) mice (cohort annotations in Figure S3C–E). We found that within the HSC population, representing ~8% of cells, that the compartment distribution was skewed with KO HSCs having enriched expression of cell cycle gene signatures ($p<10^{-63}$; Figure 1G top panel; S3F) and decreased expression of early lymphoid commitment signatures ($p<10^{-14}$; Figure 1G bottom panel; S3G) consistent with negative enrichment for cell specification. We expanded upon these findings by comparing bulk LSK differentially expressed genes to gene expression data from dormant and active HSCs separately isolated through genetic lineage tracing studies (Cabezas-Wallscheid et al., 2017). We observed that genes that were decreased in expression in *Stag2*-deficient mice were most highly expressed in slow-cycling quiescent HSCs, while the upregulated genes were most highly expressed in the proliferative MPP1 fraction (LSK, $Cd34^+$, $Flt3^-$) (Figure S3H). Similar findings were observed when comparing our data to single cell RNA-seq data, such that the most downregulated genes in *Stag2*-deficient LSKs were most highly expressed in the most quiescent HSCs (Figure S3I). Collectively, these analyses highlight a transcriptional signature associated with decreased lineage commitment, decreased quiescence, and enhanced self-renewal in the setting of STAG2 loss.

Stag2 loss impairs differentiation and induces myeloid dysplasia

To determine the consequences of these transcriptional alterations *in vivo*, we assessed the phenotype of mice with *Stag2*-deficient hematopoiesis over time. Hematopoietic-specific *Stag2* loss resulted in progressive leukopenia ($p<0.02$) and thrombocytopenia ($p<0.01$;

Figure S4A). We observed an expansion in myeloid cells and a significant reduction in B lymphocytes ($p<0.001$; Figure 2A) in the peripheral blood, which was not seen with *Stag1* deletion. *Stag2* loss, but not *Stag1* loss, induced morphologic alterations including an increase in immature myeloid cells, an expansion of small hypolobated megakaryocytes, and nuclear:cytoplasmic dyssynchrony in the erythroid lineage (Figure 2B). These abnormalities are features of human myelodysplasia—consistent with the observation that 5–15% of MDS patients have loss-of-function mutations in *STAG2* (Kon et al., 2013; Thota et al., 2014).

To determine at which level of differentiation multi-lineage dysplasia emerges, we analyzed lineage composition through analysis of scRNAseq data (Figure 2C–D). Supporting the reduction in B cell output observed in the peripheral blood, analysis of scRNAseq data showed a significant decrease in B cells and in B cell progenitors (Figure 2E). Although the paucity of lymphoid cells precluded further transcriptional tracing, we observed significant population shifts in erythroid and granulocyte development consistent with observed histologic myelodysplasia. Flow cytometric analysis of erythroblast maturation revealed attenuation at Stage III of erythropoiesis (Chen et al., 2009) (Figure 2F, S4B–C), a stage that is demarcated by condensed cell size by forward scatter (FSC) and decreased CD44 expression relative to prior stages of erythroid differentiation. *Stag2*-deficient erythroid cells were also characterized by morphologic dysplasia; immunohistochemical analysis demonstrated a marked decrease in Ter-119, a glycophorin-associated murine erythroid marker (Kina et al., 2000) (Figure 2G). By comparison, *Stag1* KO mice did not manifest hematopoietic alterations, morphologic abnormalities, or defects in erythroid differentiation (Figure S4A–C). Transcriptional analysis of the erythroid lineage in *Stag2* deficient cells further supported impaired terminal maturation ($p<10^{-44}$; Figure 2H). Genes defining this principle component define the progression from common myeloid progenitor (CMP) to megakaryocyte erythroid progenitor to erythroid A (Figure S4D–E). Overall, the most significant transcriptional difference identified in the scRNAseq was impaired granulocytic terminal maturation ($p<10^{-92}$; Figure 2I). Genes defining this principle component define the progression from CMP to GMP to granulocyte (Figure S4F–G).

Given the alterations in transcriptional output and differentiation potential, we hypothesized that *Stag2* loss led to altered chromatin accessibility at differentially expressed loci. We therefore performed RNAseq and ATAC-sequencing (ATACseq) on sorted *Stag2* WT and KO GMP and erythroid progenitor (CFU-E: Lineage$^-$cKit$^+$Sca1$^-$Cd34$^-$Fcγ^-Cd105$^+$) cells. Compared to WT GMPs, *Stag2*-deficient GMPs had enrichment for a stem-cell gene expression signature associated with increased *Evi1* expression and negative enrichment of myeloid cell development signatures by GSEA (Figure 2J). *Stag2*-deficient CFU-Es had increased expression of genes normally expressed in HSCs and in the megakaryocyte lineage, consistent with the increased self-renewal and impaired differentiation seen with Stag2 loss (Figure 2K). Integrated analysis of RNA-seq and ATAC-seq revealed that a significant subset of the downregulated genes had reduced chromatin accessibility. Both GMPs and CFU-E shared loss of accessibility and expression for genes with either CTCF/CTCFL (BORIS) or PU.1(ETS) motifs (Figure 2L–M). CTCF is a well-described cohesin binding partner (Wendt et al., 2008) that cooperates with cohesin to mediate enhancer/promoter associations (Rao et al., 2014). Notably, PU.1 and its target genes have a critical

role in determining hematopoietic lineage commitment (Antony-Debre et al., 2017; Will et al., 2015).

As we had previously reported defective lineage commitment and dynamic effects on accessibility in the heterozygous loss of *Smc3*, we compared the differentially expressed and differentially accessible genes between the two models, with the caveat that our transcriptional/epigenomic studies of *Smc3* heterozygous cells used c-kit enrichment. We identified 36 common differentially expressed genes, which were decreased in expression in both datasets. Integration of ATAC-seq data from the 2 models allowed us to identify 236 loci with altered accessibility by ATACseq in *Stag2* KO and *Smc3* heterozygous HSPC. This included 116 sites with loss of accessibility, with HOMER analysis identifying these as being highly enriched for PU.1(ETS) motifs ($p<10^{-15}$; Figure S4H). This suggests that although S*mc3* haploinsufficiency and *Stag2* loss may have non-overlapping effects on gene expression, we were able to identify alterations in gene regulation including at PU.1 target genes, consistent with an important role for the cohesin complex in hematopoietic lineage commitment.

Stag1/2 possess shared and independent chromatin binding

It has been shown using *in vitro* model systems that cohesin is essential for genomic cisinteractions and that rapid depletion of cohesin ring members result in complete loss of interphase architecture (Haarhuis et al., 2017; Rao et al., 2017; Schwarzer et al., 2017). However, these model systems do not reflect the genomic alterations observed in either human cancers or in developmental syndromes with germline cohesin mutations, such as Cornelia de Lange syndrome (Liu and Krantz, 2009). As the complete loss of cohesin structural loop components may not be compatible with a viable cell division event, the absence of transcriptional changes observed using *in vitro* systems of cohesin degradation (Schwarzer et al., 2017) may not reflect the pathophysiology of Stag2 loss of function. We next sought to determine how *Stag2*-loss affected chromatin topology in primary cells using Hi-C chromosome conformation capture in HSPCs. *Stag2* KO cells did not show alterations in topologically associating domain (TAD) boundaries, in global insulation, and did not show differences in the spatially segregated genomic regions known as A/B compartments compared to WT HSPCs (Lieberman-Aiden et al., 2009) (Figure 3A–C).

Given the lack of changes in global structure, we sought to determine if Stag2 loss would affect the ability of either CTCF or the structural cohesin components Smc1a and Smc3 to localize to canonical cohesin/CTCF binding sites (Nora et al., 2017). Chromatin immunoprecipitation sequencing revealed that the occupancy of these three proteins was largely unaffected by the presence or absence of Stag2 in HSPCs (Figure S5A–C). We hypothesized that complete loss of Stag2 might not alter higher order DNA topology due to redundancy with Stag1, particularly at CTCF bound sites. We therefore performed ChIP-seq to delineate Stag2 and Stag1 occupancy in HSPCs from *Stag2* WT and KO mice. We identified a set of peaks where Stag2 and Stag1 were bound in WT mice and where Stag1 occupancy increased in the absence of Stag2 (n=2,493; Figure 3D, S5D–E). Conversely, we identified a second set of peaks where Stag2, but not Stag1, was bound in WT HSPCs and lost in *Stag2* KO cells without compensatory Stag1 occupancy (n=10,809; Figure 3E, S5F–

G). Previous work has demonstrated CTCF-dependent and independent localization of the cohesin complex (Parelho et al., 2008; Rubio et al., 2008) which in epithelial cell lines have preferential binding sites for Stag1 and Stag2(Kojic et al., 2018). We hypothesized that altered regulation of Stag2-bound loci in WT cells which are not bound by Stag1 in WT or KO cells, were key to the altered differentiation and self-renewal seen in Stag2 KO mice. We found that loci with both Stag2 and Stag1 binding had the highest enrichment for CTCF binding (Figure 3F).

Loss of chromatin insulation impairs transcriptional output in Stag2 deficient hematopoietic progenitors

Stag1 was able to bind a subset of loci previously occupied by Stag2 or both Stag1 and Stag2 in WT cells; this included TAD boundaries determined by Hi-C (Figure 3G). By contrast, when we focused on Stag2-only bound sites, we observed locus-specific alterations in short-range interactions as calculated by the insulation metric (Crane et al., 2015). We quantified these alterations through measurement of cumulative local contacts and insulation score changes (ISC) that reflect local differences in chromosomal organization. To examine whether loss of Stag2 binding affects local chromosomal organization, we compared ISC in WT and *Stag2*KO HSPCs and identified 71,815 ISC bins that showed local chromosomal contact changes (10kb bins with insulation score change less than −0.1 or greater than 0.1, Figure S6A, left panel). We then overlapped ISC bins with Stag1/2 co-bound and Stag2-unique peaks. Annotation analysis of both Stag1/Stag2 common and Stag2-unique peaks showed enrichment of Stag2-unique ISC peaks within promoter regions compared to Stag1/Stag2 common peaks (fisher's exact test $p<3.03 \times 10^{-26}$ for ISC up; $p<1.22 \times 10^{-10}$ for ISC down; Figure S6A, right panel), suggesting that the ISC seen in *Stag2*-deficient cells may contribute to altered gene expression.

These data suggested that the role of Stag2 in gene regulation and in hematopoiesis might be due to regulation of loci bound by factors other than CTCF. To determine the impact of *Stag2* loss on chromatin structure and transcriptional output we performed RNA-seq and ATAC-seq in WT and Stag2 KO HSPCs. Similar to gene expression/ATAC-seq data in sorted hematopoietic subsets, the majority of genes with significantly altered chromatin accessibility and gene expression in the absence of *Stag2* had decreased accessibility and reduced transcription (Figure 4A). Several of the ATAC peaks with reduced accessibility were in proximity to critical B cell and myeloid lineage defining transcription factors, including *Ebf1, Pax5*, and *Cebpb*. To uncover transcription factor networks underlying these changes, we performed motif enrichment on peaks with concomitant reduction in accessibility/gene expression. We observed enrichment for Gata, Ebf, and E2A targets within the loci with decreased expression and accessibility (Figure 4B), but not for Cebpb motifs. The genes associated with loss of insulation by ISC significantly overlapped with those loci with decreased accessibility and decreased expression, with *Ebf1* and *Pax5* among the genes with the greatest magnitude of insulation change (Figure 4C, S6B–D). Notably, this effect was not confounded by sequencing depth as there were not significant differences in read counts across replicates (Figure S6E) and Hi-C contact frequencies were corrected and scaled to exclude sequencing depth bias (Crane et al., 2015). We therefore performed motif analysis on Stag1/2 common and Stag2-unique sites by dichotomizing those that were

bound and not bound by CTCF. As expected, loci with shared Stag1/Stag2 occupancy and CTCF binding sites were enriched for CTCF and CTCFL (BORIS) binding motifs. By contrast, Stag2-unique loci (not bound by Stag1) were enriched for key lineage-specific transcription factor motifs including ERG, IRF8, and PU.1 (Figure 4D). These transcription factors are essential for myeloid and lymphoid development (McKercher et al., 1996; Wang et al., 2014) and attenuated function of these transcription factors has transformative potential in murine (Will et al., 2015) and human hematopoietic cells (Mueller et al., 2006; Pogosova-Agadjanyan et al., 2013; Vangala et al., 2003).

Altered Ebf1 chromatin structure results in attenuated B-cell development in Stag2-deficient hematopoietic progenitors

We next sought to determine if the altered expression of hematopoietic transcription factors were due to alterations in the population distribution in HSPC or was due to altered expression of these factors in purified hematopoietic populations, including in MPPs antecedent to full lineage commitment. We measured *PU.1* and *Ebf1* expression and B cell differentiation in MPPs and in common lymphoid progenitors (CLP: LSK $^{+}$Cd150^{-}Cd48^{+}Cd127^{+}) from *Stag2* KO and WT mice. We found that *Ebf1* expression was reduced/absent in purified *Stag2* KO MPPs ($p<0.04$, $Log_2FC=-1.8$) and CLPs (not detectible in KO), while there was no significant difference in *PU.1* expression in either cell type (Figure 4E). Consistent with these data, B cell maturation was blocked from the pro-B cell to early pre-B cell stage (Pucella et al., 2015) in *Stag2* KO mice, with almost no late pre-B cells (Figure 5A). These findings were further bolstered by *in vitro* colony assays in B cell cytokine enriched methylcellulose where *Stag2* KO HSPCs failed to generate B cell colonies ($p<0.003$; Figure 5B). We next investigated if the same was true in Stag2-mutant MDS patients by enumerating B cells and B cell progenitors in STAG2-mutant MDS patient bone marrow samples compared to a cohort of non-MDS individuals evaluated for refractory cytopenias (Figure 5C, S6F). Immature B cells (CD34+CD19+) were decreased by 1.7-fold ($p<0.01$) in STAG2-mutant MDS patients, demonstrating that altered B-cell lineage commitment is observed in STAG2-mutant MDS.

Given that PU.1 can regulate myeloid and lymphoid lineage commitment (Scott et al., 1997) and the enrichment for PU.1 motif/targets in our epigenomic/transcriptional analysis, we investigated the role of PU.1 in Stag2-deficient alterations in B-cell lineage commitment and self-renewal. PU.1 silencing reduced B-lineage output derived from WT hematopoietic cells, similar to the effects of Stag2 deletion (Figure 5D, top row). However, the reduced B-cell lineage output of *Stag2* KO cells was not further attenuated by PU.1 silencing as assessed by flow cytometry of B220 expression (Mansson et al., 2008) and B-lineage colony formation (Figure 5D, bottom row; S6G). By contrast, overexpression of PU.1 was unable induce *Ebf1* expression in Stag2 KO cells (Figure S6H) and unable to restore B220 expression in B cell methylcellulose cultures (Figure 5D, middle row). Moreover, increased PU.1 expression did not attenuate the increased expression of the stem/progenitor marker cKit seen in *Stag2*-deficient hematopoietic cells (Figure 5E) or attenuate the capacity of *Stag2*-deficient hematopoietic cells to serially replate (Figure S6I). Given these results, we suspected that PU.1 occupancy would be affected by Stag2 loss and we performed ChIPseq for PU.1 in Stag2 WT and KO HSPC (Figure 5F). We identified 246 loci with reduced PU.1 occupancy

in Stag2 KO bone marrow. HOMER analysis confirmed that these sites contain the PU.1(ETS) motif ($p<10^{-98}$; Figure 5F–G). These data suggest that PU.1 occupancy is reduced in the absence of *Stag2*, but restored PU.1 expression is not sufficient to reverse the alterations in hematopoietic differentiation and self-renewal seen in *Stag2* KO cells.

This led us to hypothesize that key transcription factors downstream of PU.1 which are bound by Stag2 have locus specific alterations in conformation in the absence of Stag2 that lead to alterations in target gene expression with functional importance which cannot be rescued by re-expression of upstream transcription factors. *Ebf1* has three PU.1 bound sites which are decreased in Stag2 KO (Figure 5H) and four Stag2 bound sites in hematopoietic progenitors, each of which is not bound by Stag1 in WT or KO cells (Figure 6A). As noted above, we observed near-complete abrogation of *Ebf1* transcription including in MPPs preceeding Blineage commitment (Figure 4E). Although *Ebf1* expression increased in PU.1 overexpressing Stag2 WT cells ($p<0.014$), we did not observe induction of *Ebf1* expression when *PU.1* was overexpressed in *Stag2* KO cells (Figure S6H). We observed a significant reduction in local insulation throughout the *Ebf1* locus (Figure 6B) including loss of cis-interactions at three Stag2 binding sites (Figure 6C). Consistent with this hypothesis, expression of *Ebf1* in Stag2 KO progenitors (Figure S6J) restored B-lineage marker expression and B-cell colony formation *in vitro* (Figure 6D). *Ebf1*-expressing Stag2 KO progenitors had decreased cKit expression (Figure 6E) and *Ebf1* restoration abrogated the serial replating capacity of *Stag2*-deficient cells (Figure 6F). Stag2 WT and KO HSPC infected with GFP-tagged *Ebf1* were then transplanted into lethally irradiated recipients, which led to restored B cell output in vivo ($p<0.001$, Figure 6G). Taken together, these data demonstrate a key role for Stag2-mediated regulation of Ebf1 expression in modulating the balance between hematopoietic differentiation and self-renewal.

Discussion

The cohesin complex is essential in pleiotropic cellular and gene regulatory functions, including in chromosome segregation (Losada et al., 1998; Toth et al., 1999) and in maintaining DNA interactions (Rao et al., 2017; Schwarzer et al., 2017) which regulate gene expression (Cuartero et al., 2018; Kagey et al., 2010; Seitan et al., 2013). Here we demonstrate a non-redundant role of Stag2 and Stag1 in hematopoiesis, with a specific role for Stag2 in regulating the balance between hematopoietic differentiation and self-renewal. In addition, we show that Stag2 bound loci that are not bound by Stag1 undergo locus specific changes in local interactions that, in the absence of Stag2, leads to altered expression of key loci governing hematopoietic function. Taken together, these data illustrate a critical link between Stag2, DNA interactions, and gene regulation that contributes to hematopoietic transformation.

Stag2 and Stag1 have both shared and distinct roles (Kojic et al., 2018). These paralogs have a redundant role in chromatid separation such the presence of either protein within the cohesin complex is adequate for intact sister chromatid alignment. In contrast to deletion of core cohesin ring components, which abrogates the survival of hematopoietic cells (Viny et al., 2015), somatic deletion of either *Stag1* or *Stag2* was compatible with hematopoietic stem cell viability, whereas loss of both genes led to hematopoietic failure and defective

chromosomal segregation. Our *in vivo* studies underscore previous *in vitro* dependency studies (van der Lelij et al., 2017) and suggest that therapies which directly or indirectly alter Stag1 function will induce a specific dependency in Stag2 mutant cancer cells. However, increased self-renewal, impaired lineage commitment, and progressive hematopoietic alterations were observed with Stag2 deletion but not with Stag1 loss. These studies illustrate that Stag2 has a key role in hematopoiesis and in hematopoietic transformation that is not shared by Stag1. Future studies will illustrate how Stag2 loss of function cooperates with other alleles to promote leukemic transformation and how co-occurring disease alleles cooperate with the chromatin architecture alterations induced by *Stag2* loss.

Our data suggest that the role of Stag2 in regulating hematopoiesis and in hematopoietic transformation is Stag1-independent. Key hematopoietic regulators which show differential expression, accessibility, and insulation in the absence of Stag2 are bound by Stag2 and not by Stag1. This includes several key genes essential for lineage commitment to lymphoid fate, including the PU.1 targets *Ebf1* and *Pax5*. Previous studies demonstrated that PU.1-mediated regulation of *Ebf1* is a key event in B-cell lineage commitment (Medina et al., 2004; Scott et al., 1997), and PU.1 has been defined to be a pioneer factor with nucleosome remodeling capacity. Given these data and the known role of Ebf1 in B cell commitment/differentiation (Zandi et al., 2008), we show that PU.1 restoration cannot rescue the impact of Stag2 loss on hematopoietic self-renewal and lineage commitment and point to non-hierarchical roles for transcription factor expression and the permissive chromatin context regulated by Stag2. By contrast, restoration of Ebf1 expression restores differentiation and abrogates the aberrant self-renewal of Stag2 deficient cells.

Our data illustrate a key role for Stag2 in the balance between self-renewal and differentiation, a critical feature of transformation across different tumor types. Moreover, the observation that reactivation of the Stag2-target Ebf1 can reverse these alterations suggests a key role for Stag2-regulated transcription factor networks in tumor suppression, which is reversible when key networks are restored in Stag2 mutant cells. We hypothesize that Stag2 loss-of-function induces lineage specific alterations in transcription factor function in a spectrum of malignant contexts. Most importantly, our studies identify a key pathophysiologic role for mutations in the factors that govern gene regulatory architecture in malignant transformation. Our data point to the reversibility of transcriptional dysregulation which mediates aberrant self-renewal and differentiation in cancer cells and suggest that therapies that reverse these alterations may have therapeutic benefit in cohesin-mutant cancers.

STAR Methods

Lead Contact and Materials Availability

Further information and requests for resources and reagents should be directed to and will be fulfilled by the Lead Contact, Ross L. Levine (leviner@mskcc.org).

Mouse lines generated in this study have been deposited to Jackson Laboratory (Jax), *Stag2*^{flox} (JAX#030902); *Stag1*^{flox} (JAX#030904).

Experimental Models and Subject Details

Animals—All animals were housed at Memorial Sloan Kettering Cancer Center. All animal procedures were conducted in accordance with the Guidelines for the Care and Use of Laboratory Animals and were approved by the Institutional Animal Care and Use Committees at Memorial Sloan Kettering Cancer Center.

Generation of Stag1/2-deficient mice—The *Stag2* and *Stag1* conditional allele were each deleted by targeting exon 7. Two *LoxP* sites flanking exon 7 and an *Frt*-flanked neomycin selection cassette were inserted in the upstream intron (Figure S1A). 10 μg of the targeting vector was linearized by NotI and then transfected by electroporation of BAC-BA1 (C57BL/6 × 129/SvEv) hybrid ES cells. After selection with G418 antibiotic, surviving clones were expanded for PCR analysis to identify recombinant ES clones. Secondary confirmation of positive clones identified by PCR was performed by Southern blotting analysis. DNA was digested with BamHI and electrophoretically separated on a 0.8% agarose gel. After transfer to a nylon membrane, the digested DNA was hybridized with a probe targeted against the 3′ or 5′ external region. DNA from C57BL/6 (B6), 129/SvEv (129), and BA1 (C57BL/6 × 129/SvEv; Hybrid) mouse strains was used as WT controls. Positive ES clones were expanded and injected into blastocysts. The generated mice ($Stag2^{fl/fl}$ and $Stag1^{fl/fl}$) were initially crossed to a germline *Flp*-deleter (The Jackson Laboratory), to eliminate the neomycin cassette, and subsequently to the IFN-α–inducible *Mx1-cre* (The Jackson Laboratory) (Kuhn et al., 1995; Lakso et al., 1996). Mice were backcrossed for six generations to C57BL/6 mice. $Stag2^{fl/fl\ or\ y}$, $Stag2^{fl/+\ or\ y}$, and $Stag2^{+/+\ or\ y}$ littermate mice were genotyped by PCR with primers Stag2-NF (5′-CACTCATGCTGGCAAGTATTGTAC-3′) and Stag2-NR (5′-AACAGCCTGAGCAAAGAATCCAAAG-3′) and Stag2–3' (5′-TGTGTGCCTCTTTGAACAATGCCC-3′) using the following parameters: 94°C for 3 min, followed by 35 cycles of 94°C for 15 s, 64°C for 30 s, and 72°C for 90 s, and then 72°C for 5 min. The WT allele was detected as a band at 385 bp, whereas the floxed allele was detected as a band of 554 bp. Excision after Cre recombination was confirmed by PCR with primers to detect a band at 294 bp. $Stag1^{fl/fl}$, $Stag1^{fl/+}$, and $Stag1^{+/+}$ littermate mice were genotyped by PCR with primers Stag1-CommonF (5′-GACTGGTATCTGACGGCTTATACC-3′) and Stag1-CommonR (5′-CACTGAGGACCAGGCATTGTAAGG-3′) and Stag1-FloxR (5′-TGAACTGATGGCGAGCTCAGACC-3′) using the following parameters: 94°C for 3 min, followed by 35 cycles of 94°C for 15 s, 62°C for 30 s, and 72°C for 90 s, and then 72°C for 5 min. The WT allele was detected as a band at 1104 bp, whereas the floxed allele was detected as a band of 745 bp. Excision after Cre recombination was confirmed by PCR with primers to detect a band at 619 bp.

Patient Samples—Diagnostic bone marrow flow cytometric data was accessed from patients seen at Memorial Sloan Kettering Cancer Center with STAG2-mutant myelodysplastic syndrome or non-STAG2 mutant patients with refractory cytopenias. Patient characteristics are depicted in Table S1. This study was approved by Institutional Review Board at the MSKCC (protocol #16–1591).

Method Details

In vivo experiments—*Mx1-cre*$^{+}$ *Stag2*$^{fl/fl}$ conditional KO and Cre^{-} *Stag2*$^{fl/fl}$ control WT mice or *Mx1-cre*$^{+}$ *Stag1*$^{fl/fl}$ conditional KO and Cre^{-} *Stag1*$^{fl/fl}$ control WT mice received four intraperitoneal injections of polyinositric:polycytidinic acid (PIpC) every other day at a dose of 20 mg/kg of body weight starting at 6 weeks after birth. Deletion/recombination was confirmed 2 weeks after PIPC injection and mice were used for experiments at least 8 weeks after PIPC injection. All mice were analyzed between 8 and 60 weeks of age. BM, spleen, and peripheral blood were analyzed by flow cytometry. Formalin-fixed paraffin-embedded tissue sections were stained with hematoxylin and eosin (H&E). Peripheral blood was smeared on a slide and stained using the Wright-Giemsa staining method. Tissue sections and blood smears were evaluated by a hematopathologist (B. Durham). Deletion of the *Stag1 and Stag2* allele and transcript was measured by genomic PCR, qRT-PCR, and Western blot analysis (described below). All experiments were repeated and results confirmed in male *Mx1-cre*$^{+}$ *Stag2*$^{fl/y}$ conditional KO and Cre^{-} *Stag2*$^{fl/y}$ control WT mice.

BM transplantation—Freshly dissected femurs and tibias were isolated from *Stag1*$^{fl/fl}$ and *Stag2*$^{fl/fl}$ CD45.2^{+} or *Mx1-cre*$^{+}$ *Stag1*$^{fl/fl}$ and *Stag2*$^{fl/fl}$ CD45.2^{+} mice. Bones were transected at the epiphyses and were centrifuged at 4°C to extract whole bone marrow int o PBS and RBCs were lysed in ammonium chloride-potassium bicarbonate lysis buffer for 10 min. After centrifugation, cells were resuspended in PBS plus 3% FBS, passed through a cell strainer, and counted. Finally, 0.5×10^6 total BM cells from *Stag1*$^{fl/fl}$ and *Stag2*$^{fl/fl}$ CD45.2^{+} or *Mx1-cre*$^{+}$ *Stag1*$^{fl/fl}$ and *Stag2*$^{fl/fl}$ CD45.2^{+} mice were mixed with 0.5×10^6 WT CD45.1^{+} support BM and transplanted via tail vein injection into lethally irradiated (two times 450 cGy) CD45.1^{+}host mice. Recipient mice were B6.SJL-Ptprc^{a}/BoyAiTac female mice between 6–12 weeks of age. Mice were purchased from Taconic. Chimerism was measured by FACS in peripheral blood at 4 weeks after transplant (week 0, pre-PIpC). Chimerism was followed via FACS in the peripheral blood every 4 weeks (week 0, 4, 6, 8, 12, and 16 after PIpC injection). Additionally, for each bleeding, whole blood cell counts were measured on a blood analyzer, and peripheral blood smears were scored. Chimerism in the BM and spleen was evaluated at 16 weeks via animal sacrifice and subsequent FACS analysis.

In vitro colony-forming assays—BM of *Stag1*$^{fl/fl}$ and *Stag2*$^{fl/fl}$ and littermate *Mx1-cre Stag1*$^{fl/fl}$ and *Stag2*$^{fl/fl}$ mice were extracted and seeded at a density of 20,000 cells/replicate into cytokine-supplemented methylcellulose medium (Methocult M3434; STEMCELL Technologies) or methylcellulose medium for mouse pre-B cells (M3630) supplemented with FLT3L (20 ng/mL), SCF (100 ng/mL), and IL7 (10 ng/mL)(de Boer et al., 2011). Colonies propagated in culture were scored at day 7. Representative colonies were isolated from the plate for cytospins and flow cytometry. Remaining cells were resuspended and counted, and a portion was taken for replating (20,000 cells/replicate) for a total of eight platings. Cytospins were performed by resuspending in warm PBS and spun onto the slides at 350 *g* for 5 min. Slides were air-dried and stained using the Giemsa-Wright method.

Antibodies, FACS, and Western blot analysis—Antibody staining and FACS analysis was performed as previously described (Abdel-Wahab et al., 2013). BM or spleen

mononuclear cells were stained with a lineage cocktail comprised of antibodies targeting CD4, CD8, B220, NK1.1, Gr-1, CD11b, and Ter119. Cells were also stained with antibodies against c-Kit, Sca-1, IL-7Rα, FcγRII/III, and CD34. Cell populations were analyzed using a Fortessa Flow Cytometer (BD) and sorted with a FACS-SH800 instrument (Sony). All FACS antibodies were purchased from BD or eBioscience. We used the following antibodies: c-Kit (2B8), Sca-1 (D7), Mac-1/CD11b (M1/70), Gr-1 (RB6–8C5), NK1.1 (PK136), Ter-119, IL7-Rα (A7R34), IgD (11–26c.2a), IgM (RMM-1), CD34 (RAM34), FcγRII/III (2.4G2), CD4 (RM4–5), CD8 (53–6.7), CD19 (HIB19), CD43 (1B11), CD44 (IM7), CD45.1 (A20), CD45.2 (104), CD45R/B220 (RA3–6B2), CD71 (R17217), CD105 (MJ7/18), CD150 (9D1), and CD48 (HM48–1). The following antibodies were used for Chromatin Immunoprecipitation and Western blot analysis: Stag2 (Bethyl, A302–580A), Stag1 (Bethyl, A302–579A), Smc3(Bethyl, A300–060A), Smc1a (Active Motif, 61067), Ctcf (Cell Signaling, 3418S), PU.1 (Cell Signaling, #2266S), and Actin (CalBiochem, JLA-20).

Multiparameter flow cytometry was performed on bone marrow aspirates at diagnosis for patients with STAG2 mutant MDS and matched controls patients with nonmalignant cytopenias. Briefly, up to 1.5 million cells from freshly drawn bone marrow aspirate were stained with a 10-”color” panel (CD15-FITC, CD33-PE, CD117-PC5, CD13-PE-Cy7, CD34-APC, CD71-APC-A700, CD38-APC-A750, HLA-DR-PAC Blue, CD45-V500C, and CD19-BV605), washed, and acquired on a Canto-10 cytometer (BD Biosciences, San Jose, CA). The results were analyzed with custom Woodlist software (generous gift of Wood BL, University of Washington). In order to enumerate the B cells, CD19+CD15-CD33-CD13-cells were gated. Plasma cells were excluded based on the bright CD38 expression. CD34+/CD19+ cells were considered as immature B cells.

Histological analyses—Mice were sacrificed and autopsied, and dissected tissue samples were fixed for 24 h in 4% paraformaldehyde, dehydrated, and embedded in paraffin. Paraffin blocks were sectioned at 4 μm and stained with H&E. Images were acquired using an Axio Observer A1 microscope (Carl Zeiss).

Peripheral blood analysis—Blood was collected by submandibular bleeding using a 5mm lancet (MEDipoint Inc). Automated peripheral blood counts were obtained using a ProCyte Dx (IDEXX Laboratories) according to standard manufacturer’s instruction. Differential blood counts were realized on blood smears stained using Wright-Giemsa staining and visualized using an Axio Observer A1 microscope.

Cytogenetic Analysis and Metaphase Karyotyping—Bone marrow acquired at necropsy was resuspended in cytokine enriched media containing 5mL RPMI 10% FCS supplemented with 2mM L-glutamine and after documented excision or 8 weeks after PIpC. Harvested cells were cultured in T25 tissue culture flasks with 25 uL of Colcemid (10mg/mL) (Gibco Life Technologies, Inc) for 45 minutes and 4 hours respectively, resuspended in 0.075 mol/L KCl for 10 minutes at 37°C and fixed in methanol-acetic acid (3:1). Metaphases were scored and counted. Chromosome analysis was performed on a minimum of 20 DAPI-banded metaphases and all metaphases were fully karyotyped. Low depth whole genome sequencing was performed to assess genome wide copy number. One microgram of genomic DNA was sheared using an E220 Sonicator (Covaris) to +/− 300bps.

Fragmented DNA was end-repaired, A-tailed, and ligated to Illumina TruSeq dual indexed adaptors using standard methods. Indexed libraries were enriched by PCR amplified, quantified, pooled and sequenced in multiplex fashion on an Illumina HiSeq instrument to obtain roughly 1 million sequencing reads per sample, sufficient to call copy number variation at a bin resolution of 150kb) (Baslan et al., 2015). Data was processed for copy number analysis as described previously (Baslan et al., 2012).

PU.1/EBF1 overexpression and knockdown—Lentiviral constructs expressing PU.1-IRES-GFP, PU.1 shRNA-IRES-GFP, and GFP alone were generously provided by the laboratory of Dr. Ulrich Steidl (Steidl et al., 2006; Will et al., 2015). Whole BM was negatively selected for lineage markers using antibodies conjugated to magnetic beads and separated using EasySep Mouse Hematopoietic Progenitor Cell Isolation Kit (STEMCELL Technologies). Lineage depleted BM cells were transduced at a cell density of 5×10^5 using virus concentrated through ultracentrifugation. After 48h cells were sorted for GFP expression. Overexpression/knockdown was confirmed using qRT-PCR. Retroviral constructs expressing EBF1-IRES-GFP and GFP alone were generously provided by the laboratory of Dr. Charles Mulligan. Lineage depleted BM cells were transduced at a cell density of 5×10^5 using virus concentrated using Retro-X concentrator (Clontech). After 48h cells were sorted for GFP expression and either used for *in vitro* assays or resuspended in PBS and tail-vein injected into lethally irradiated recipient mice. Blood and BM of transplanted mice were analyzed by flow cytometry as above. Overexpression was confirmed using qRT-PCR.

RNA-Seq and quantitative real-time PCR analysis—For qRT-PCR experiments, all samples were prepared in biologic triplicate. Whole BM was negatively selected for lineage markers using antibodies conjugated to magnetic beads and separated using EasySep Mouse Hematopoietic Progenitor Cell Isolation Kit (STEMCELL Technologies). Total RNA was isolated using the Trizol (Invitrogen), and cDNA was synthesized using the Verso cDNA Synthesis kit (Fisher). Quantitative PCR was performed using Taqman reagents and probes (Thermo Fisher) for ActinB (Mm02619580_g1), Spi1, (Mm00488140_m1) and Ebf1 (Mm00432948_m1) and FastStart Universal SYBR Green (Sigma) and primers for Stag2 (F: 5'-TGCTATGCAGTCGGTGGTAG-3') and (R: 5'-AGGACCAGCCATGGTAAGTG-3'), Stag1 (F: 5'-CTACAAGCATGACCGGGACAT-3') and (R: 5'-AGGGTACTTGTATGCCTAAAAGC-3'), and ActinB (F: 5'-GGCTGTATTCCCCTCCATCG-3') and (R: 5'-CCAGTTGGTAACAATGCCATGT-3'). For mRNA-Seq analysis, samples were prepared and analyzed in biologic triplicate. For RNA-sequencing, RNA was isolated by TriZOL extraction from sorted-cell population or lineage negative bone marrow as indicated. RNA-sequencing libraries were generated by 3' sequencing and SMART-Seq2 amplification and sequenced on an Illumina NextSeq 500.

Single cell RNA-sequencing and data analysis—Lineage$^-$bone marrow cells from 3 Stag2 WT and 3 Stag2 KO mice were sorted for viability (4′,6-diamidino-2-phenylindole (DAPI)-negative). Individual samples were loaded on 10X Genomics Chromium System aiming to generate 7,000 Gel Beads in Emulsion (GEMs) per sample. scRNA-seq libraries were prepared following 10X Genomics protocols (Chromium Single Cell 3' Reagent Kits

User Guide v2 Chemistry). Libraries were sequenced on NovaSeq 6000 (Illumina) system (S2 flow cell, paired-end) recovering a median of 239,350,330 reads/sample.

ATAC-sequencing—Chromatin accessibility assays utilizing the bacterial Tn5 transposase were performed as described (Corces et al., 2016) with minor modifications. Cells (1.0×10^4) were lysed and incubated with transposition reaction mix containing PBS, 1% Digitonin, Tween-20, and Transposase (llumina). Samples were incubated for 30 minutes at 37°C in a thermomixer at 1000rpm. Prior to amplification, samples were concentrated with the DNA Clean and Concentrator Kit-5 (Zymo). Samples were eluted in 20uL of elution buffer and PCR-amplified using the NEBNext 2X Master Mix (NEB) for 10 cycles and sequenced on a NextSeq 500 (Illumina).

Chromatin Immunoprecipitation-sequencing—Cells (~0.5–1 million cells were used for one ChIP reaction) were cross-linked with 1% formaldehyde (Sigma, F1635) at 37°C for 12 min, inv erting occasionally, and quenched with 1.25 M glycine and Tris-HCl and placed on ice. Cells pellets were washed with cold PBS and transferred to Eppendorf tubes. Cell pellets were resuspended in 1ml SDS lysis buffer (1% SDS, 10mM EDTA, 50mM Tris-HCl pH8) containing proteinase inhibitor and centrifuged at maximum speed for 10 minutes at room temperature. After aspirating the supernatant, the pellet was resuspended in 130uL ChIP buffer supplemented with protease inhibitor and transferred to a AFA microtube (Covaris). Sonication was performed on a E220 Sonicator (Covaris) for 360 seconds using manufacturer settings (Peak Power 105, 200 Cycles/burst, Duty Factor 3). ChIP inputs were decrosslinked by adding 5M NaCl and 0.1X TE and incubated overnight at 65C followed by bead purification with AMPure XP beads (Beckman Coulter). Sonicated chromatin was incubated with primary antibody 1:50 total volume of chromatin and incubated overnight, rotating at 4C. Dyna beads prewashed in ChIP buffer were added at 5X volume of antibody and incubated for 3 hours rotating at 4C and then washed with salt buffers mixed micelle, B500, LiCl, and TBS. The ChIP product was then eluted from the Dynabeads in 52uL elution buffer and incubating for 15 minutes. ChIP product was decrosslinked with 2uL 5M NaCl and incubated overnight at 65C. Libraries were prepared using the NEBNext® ChIP-seq Library Prep Master Mix Set for Illumina ® (NEB, E6240L) and Swift Accel-NGS® 2S Plus and Swift Accel-NGS® 2S MID Indexed adapters. Samples were QC'd using a Bioanalyzer TapeStation (Agilent Technologies 2200) to determine fragment size. Samples were pooled and submitted for SE50 sequencing using an Illumina NextSeq500.

Hi-C—Hi-C was performed as previously described (Belaghzal et al., 2017). Briefly, Lin^- bone marrow cells (5×10^6) were cross-linked in 1% formaldehyde for 10 minutes and quenched in 125mM glycine. Cross-linked cells were lysed in Hi-C lysis buffer (10mM Tris-HCl pH8.0, 10mM NaCl, 0.2% Igepal CA-630 and Halt protease inhibitors Thermo Fisher 78429). After disruption, chromatin was solubilized and digested using 400Units of DpnII at 37°C overnight. DNA overhangs were then filled in with biotin-14-dATPs and ligated with T4 ligases at 16°C for 4 hours. Cross-links of ligated DNAs were reversed with proteinase K (Life Technologies, 25530–031) at 65°C overnight and purified using phenol:ch olorform. After removal of biotin from unligated ends, DNA was fragmented to 150–350 bps using an E220 sonicator (Covaris). After end repair, biotinylated DNA was collected using

streptavidin beads (MyOne C1 beads, Life Technologies, 650.01) to prepare Hi-C libraries using the Illumina TruSeq Nano DNA kit. Hi-C libraries were sequenced on an Illumina NextSeq500 and raw sequencing data in the Fastq format were obtained.

Experimental Design—No specific methods were used for randomization and investigators were not blinded to the identity of samples. No statistical methods were utilized to determine sample size. The experiments described in this study were designed to use the minimum number of animals required. Each experiment was performed using separate cohorts for males and females, both in triplicate, to ensure reproducibility.

Quantification and Statistical Analysis

In vivo experiments—The number of animals, cells and experimental replication can be found in the respective figure legend. The unpaired Student's t test was used to compare the mean of two groups. Data were analyzed and plotted using GraphPad Prism 6 software. Data shown in graphs indicate mean ± S.D. Kaplan-Meier survival analysis and log-rank test were used to compare survival outcomes.

RNA-Seq data analysis—Fastq files were mapped to the mouse genome (mm9) and reads counts per gene were quantified using STAR(Dobin et al., 2013) with default parameters and genecode (vM1) annotation file. Differentially expressed genes (DEGs) were identified with DESeq2 (Love et al., 2014), with a fold change cutoff of +/− 2 and a FDR of 10%. Motif enrichment on DEGs was performed with HOMER using a window of −1kb to +100bp around the transcription start site. Gene ontology analysis was also performed using HOMER.

Single cell RNA-sequencing and data analysis—FASTQ files were processed using the Sequence Quality Control (SEQC) pipeline (Azizi et al., 2018) and reads were aligned to the mouse genome mm38, resulting in a median of 4226 cells/samples with a median of 5036 molecules/cell. Cells from the lower molecule counts, determined by lower mode of molecule counts distribution (5.8% of cells), were additionally filtered out to remove putative empty droplets, resulting in a final collection of 24,153 cells. The resulting count matrices from all samples were then combined and normalized to median library-size and log transformed shown in Figures 1G, 2C–D and S4C. For individual subsets of granulocytes, MEP, HSCs, cells were normalized within the subset. Ribosomal genes were excluded in downstream analyses. In the global cohort, t-SNE was performed on 20 principal components, explaining ~83.6% of data variance, with a perplexity of 150. For subpopulations analyses, the number of PCs considered was determined based on the knee point of explained variance (granulocytes: 8, MEP: 14, HSC: 7) and perplexity was fixed at 150.

In order to annotate principal components (Figure 1G, 2H, 2I), the Pearson correlation between each principal component and expression of gene signatures was computed. Gene lists were sorted by correlation and ranked Gene Set Enrichment Analysis (GSEA) was performed. In addition, expression of most correlated and anticorrelated was assessed in

bulk RNA-sequencing data of sorted populations to identity components defined by lineage maturation.

To annotate subsets of cells, we performed clustering of normalized and log transformed data using Phenograph (Levine et al., 2015). Then, Pearson correlation between the centroid of each cluster and standardized bulk RNA-seq data on sorted subsets (from Haemopedia-Mouse RNAseq,(de Graaf et al., 2016)) was computed (Figure S3D). The subset with highest correlation to each cluster was used to annotate the cluster, as shown in Figures 2D, S3D. The cluster annotations were confirmed through studying differentially expressed genes in each cluster. Differential expression analysis was performed using the Wasserstein distance (Santambrogio and SpringerLink (2015)) between normalized and log-transformed expression in cells from each inferred lineage and all other cells (Figure S3E).

Epigenomic data analysis—Reads were trimmed for both quality and Illumina adapter sequences using ‘trim_galore’ then aligned to mouse assembly mm9 with bowtie2 using the default parameters. Aligned reads with the same start site and orientation were removed using the Picard tool MarkDuplicates (http://broadinstitute.github.io/picard). ChIP density profiles were created by extending each read to the average library fragment size and then computing density using the BEDTools suite (http://bedtools.readthedocs.io). Reads were not extended when generating ATAC-seq read density. Enriched regions were discovered using MACS2 and scored against matched input libraries (fold change > 2 and p-value < 0.005). Peaks were then filtered against genomic ‘blacklisted’ regions (http://mitra.stanford.edu/kundaje/akundaje/release/blacklists/mm9-mouse/mm9-blacklist.bed.gz) and filtered peaks within 500 bp were merged to create a full peak atlas. Raw read counts were tabulated over this peak atlas using featureCounts (http://subread.sourceforge.net). All genome browser tracks and read density tables were normalized to a sequencing depth of ten million mapped reads. Peaks were annotated using linear genomic distance, with a gene assigned to a peak if it was within 50 kb upstream or downstream of the gene start or end, respectively. Motif signatures were obtained using the ‘de novo’ approach in Homer v4.5 (http://homer.ucsd.edu). Rescued peaks were defined as Stag2 regions in which Stag1 was enriched above input in the Stag2 KO, whereas non-rescued peaks showed no evidence of Stag1 binding in the Stag2 KO background.

Hi-C—Hi-C data was processed based on the previous method(Belton et al., 2012). Fastq files were mapped binned using c-World pipeline from the Dekker lab, which is available at a GitHub repository(Lajoie et al., 2015), https://github.com/dekkerlab/cMapping; https://github.com/dekkerlab/balance; https://github.com/dekkerlab/cworld-dekker). Briefly, 50bp paired end reads were truncated to 25bp starting at the 5-prime end and then were iteratively mapped onto mm9. Uniquely mapped, paired end reads were collected and assigned to DpnII restriction fragments based on their 5-prime locations. Mapped reads with same fragment ends and uniqueness were kept, and PCR duplicates were removed. Interaction heat-maps, insulation scores and loop pile-up were generated using scripts included in c-world pipeline. The loop coordinates used for loop pileup analysis were obtained from the mouse CH12.LX line(Rao et al., 2014). To increase resolution of Hi-C interaction profiles, intermediate validpairs files from the same genotype mice were pooled together using

cooltools from the Mirny Lab (https://github.com/mirnylab). The insulation score change (ISC) between *Stag2*$^{-/y}$ and *Stag2*$^{fl/y}$ was calculated using 10kb binned Hi-C data and the ISC bins containing Stag2 rescued or non-rescued peaks were identified with Bedtools and annotated using ChIPseeker (Yu et al., 2015).

Data and Code Availabilities

The ATACseq, RNAseq, scRNAseq, ChIPseq, and Hi-C datasets generated during this study are available and deposited on Gene Expression Common under accession number GEO: 134583

Supplementary Material

Refer to Web version on PubMed Central for supplementary material.

Acknowledgments

We acknowledge the use of the Integrated Genomics Operation Core, funded by the MSKCC Support Grant NIH P30 CA008748, and the Marie-Josée and Henry R. Kravis Center for Molecular Oncology. We would like to thank Dr. Gouri Nandakumar and the staff of the Cytogenetics Core Facility for their assistance in imaging and processing of 5 cytogenetic data.

Funding: This work was supported by National Cancer Institute awards R35 CA197594–01A1 (RLL), R01 CA216421 (RLL), and PS-OC U54 CA143869–05 (RLL and JD) and a grant from Leukemia & Lymphoma Society Translational Research Foundation 6499–17 (RLL). ADV is supported by a National Cancer Institute career development grant K08 CA215317, the William Raveis Charitable Fund Fellowship of the Damon Runyon Cancer Research Foundation (DRG 117–15), and an EvansMDS Young Investigator grant from the Edward P. Evans Foundation. RLB is supported by the Sohn Foundation Fellowship of the Damon Runyon Cancer Research Foundation (DRG 22–17). TB is supported by the William C. and Joyce C. O'Neil Charitable Trust, MSKCC Single Cell Sequencing Initiative. J.D. is an investigator of the Howard Hughes Medical Institute.

Declaration of interests: ADV received travel support from Mission Bio and is on the Editorial Advisory Board of Hematology News. JD is on the Scientific Advisory Board of Arima Genomics, and a consultant for Omega Therapeutics. RLL is on the supervisory board of Qiagen and is a scientific advisor to Loxo, Imago, C4 Therapeutics and Isoplexis. He receives research support from and consulted for Celgene and Roche and has consulted for Janssen, Astellas, Morphosys and Novartis. He has received honoraria from Roche, Lilly and Amgen for invited lectures and from Gilead for grant reviews. RLB, YL, WX, BHD, SEE, AN, ISC, MW, EA, TB, CJO, and RK have nothing to disclose.

Reference

Abdel-Wahab O, Gao J, Adli M, Dey A, Trimarchi T, Chung YR, Kuscu C, Hricik T, Ndiaye-Lobry D, Lafave LM, et al. (2013). Deletion of Asxl1 results in myelodysplasia and severe developmental defects in vivo. The Journal of experimental medicine 210, 2641–2659. [PubMed: 24218140]

Adolfsson J, Borge OJ, Bryder D, Theilgaard-Monch K, Astrand-Grundstrom I, Sitnicka E, Sasaki Y, and Jacobsen SE (2001). Upregulation of Flt3 expression within the bone marrow Lin(−)Sca1(+)c-kit(+) stem cell compartment is accompanied by loss of self-renewal capacity. Immunity 15, 659–669. [PubMed: 11672547]

Antony-Debre I, Paul A, Leite J, Mitchell K, Kim HM, Carvajal LA, Todorova TI, Huang K, Kumar A, Farahat AA, et al. (2017). Pharmacological inhibition of the transcription factor PU.1 in leukemia. J Clin Invest 127, 4297–4313. [PubMed: 29083320]

Azizi E, Carr AJ, Plitas G, Cornish AE, Konopacki C, Prabhakaran S, Nainys J, Wu K, Kiseliovas V, Setty M, et al. (2018). Single-Cell Map of Diverse Immune Phenotypes in the Breast Tumor Microenvironment. Cell 174, 1293–1308 e1236. [PubMed: 29961579]

Bailey ML, O'Neil NJ, van Pel DM, Solomon DA, Waldman T, and Hieter P (2014). Glioblastoma cells containing mutations in the cohesin component STAG2 are sensitive to PARP inhibition. Mol Cancer Ther 13, 724–732. [PubMed: 24356817]

Balbas-Martinez C, Sagrera A, Carrillo-de-Santa-Pau E, Earl J, Marquez M, Vazquez M, Lapi E, Castro-Giner F, Beltran S, Bayes M, et al. (2013). Recurrent inactivation of STAG2 in bladder cancer is not associated with aneuploidy. Nat Genet 45, 1464–1469. [PubMed: 24121791]

Baslan T, Kendall J, Rodgers L, Cox H, Riggs M, Stepansky A, Troge J, Ravi K, Esposito D, Lakshmi B, et al. (2012). Genome-wide copy number analysis of single cells. Nat Protoc 7, 1024–1041. [PubMed: 22555242]

Baslan T., Kendall J., Ward B., Cox H., Leotta A., Rodgers L., Riggs M., D'Italia S., Sun G., Yong M., et al. (2015). Optimizing sparse sequencing of single cells for highly multiplex copy number profiling. Genome Res 25, 714–724. [PubMed: 25858951]

Belaghzal H, Dekker J, and Gibcus JH (2017). Hi-C 2.0: An optimized Hi-C procedure for high-resolution genome-wide mapping of chromosome conformation. Methods 123, 56–65. [PubMed: 28435001]

Belton JM, McCord RP, Gibcus JH, Naumova N, Zhan Y, and Dekker J (2012). Hi-C: a comprehensive technique to capture the conformation of genomes. Methods 58, 268–276. [PubMed: 22652625]

Benedetti L, Cereda M, Monteverde L, Desai N, and Ciccarelli FD (2017). Synthetic lethal interaction between the tumour suppressor STAG2 and its paralog STAG1. Oncotarget 8, 37619–37632. [PubMed: 28430577]

Cabezas-Wallscheid N, Buettner F, Sommerkamp P, Klimmeck D, Ladel L, Thalheimer FB, Pastor-Flores D, Roma LP, Renders S, Zeisberger P, et al. (2017). Vitamin A-Retinoic Acid Signaling Regulates Hematopoietic Stem Cell Dormancy. Cell 169, 807–823 e819. [PubMed: 28479188]

Cancer Genome Atlas Research, N., Ley TJ, Miller C, Ding L, Raphael BJ, Mungall AJ, Robertson A, Hoadley K, Triche TJ Jr., Laird, PW, et al. (2013). Genomic and epigenomic landscapes of adult de novo acute myeloid leukemia. N Engl J Med 368, 2059–2074. [PubMed: 23634996]

Chen K, Liu J, Heck S, Chasis JA, An X, and Mohandas N (2009). Resolving the distinct stages in erythroid differentiation based on dynamic changes in membrane protein expression during erythropoiesis. Proc Natl Acad Sci U S A 106, 17413–17418. [PubMed: 19805084]

Corces MR, Buenrostro JD, Wu BJ, Greenside PG, Chan SM, Koenig JL, Snyder MP, Pritchard JK, Kundaje A, Gkeenleaf WJ, et al. (2016). Lineage-specific and single-cell chromatin accessibility charts human hematopoiesis and leukemia evolution. Nature Genetics 48, 1193–1203. [PubMed: 27526324]

Crane E, Bian Q, McCord RP, Lajoie BR, Wheeler BS, Ralston EJ, Uzawa S, Dekker J, and Meyer BJ (2015). Condensin-driven remodelling of X chromosome topology during dosage compensation. Nature 523, 240–244. [PubMed: 26030525]

Cuartero S, Weiss FD, Dharmalingam G, Guo Y, Ing-Simmons E, Masella S, Robles-Rebollo I, Xiao X, Wang YF, Barozzi I, et al. (2018). Control of inducible gene expression links cohesin to hematopoietic progenitor self-renewal and differentiation. Nat Immunol.

de Boer J, Yeung J, Ellu J, Ramanujachar R, Bornhauser B, Solarska O, Hubank M, Williams O, and Brady HJ (2011). The E2A-HLF oncogenic fusion protein acts through Lmo2 and Bcl-2 to immortalize hematopoietic progenitors. Leukemia 25, 321–330. [PubMed: 21072044]

de Graaf CA, Choi J, Baldwin TM, Bolden JE, Fairfax KA, Robinson AJ, Biben C, Morgan C, Ramsay K, Ng AP, et al. (2016). Haemopedia: An Expression Atlas of Murine Hematopoietic Cells. Stem Cell Reports 7, 571–582. [PubMed: 27499199]

Dixon JR, Selvaraj S, Yue F, Kim A, Li Y, Shen Y, Hu M, Liu JS, and Ren B (2012). Topological domains in mammalian genomes identified by analysis of chromatin interactions. Nature 485, 376–380. [PubMed: 22495300]

Dobin A, Davis CA, Schlesinger F, Drenkow J, Zaleski C, Jha S, Batut P, Chaisson M, and Gingeras TR (2013). STAR: ultrafast universal RNA-seq aligner. Bioinformatics 29, 15–21. [PubMed: 23104886]

Ferrari F, Bortoluzzi S, Coppe A, Basso D, Bicciato S, Zini R, Gemelli C, Danieli GA, and Ferrari S (2007). Genomic expression during human myelopoiesis. BMC Genomics 8, 264. [PubMed: 17683550]

Grover A, Sanjuan-Pla A, Thongjuea S, Carrelha J, Giustacchini A, Gambardella A, Macaulay I, Mancini E, Luis TC, Mead A, et al. (2016). Single-cell RNA sequencing reveals molecular and functional platelet bias of aged haematopoietic stem cells. Nat Commun 7, 11075. [PubMed: 27009448]

Haarhuis JHI, van der Weide RH, Blomen VA, Yanez-Cuna JO, Amendola M, van Ruiten MS, Krijger PHL, Teunissen H, Medema RH, van Steensel B, et al. (2017). The Cohesin Release Factor WAPL Restricts Chromatin Loop Extension. Cell 169, 693–707 e614. [PubMed: 28475897]

Herman JS, Sagar, and Grun D (2018). FateID infers cell fate bias in multipotent progenitors from single-cell RNA-seq data. Nat Methods 15, 379–386. [PubMed: 29630061]

Jiang J, Yu H, Shou Y, Neale G, Zhou S, Lu T, and Sorrentino BP (2010). Hemgn is a direct transcriptional target of HOXB4 and induces expansion of murine myeloid progenitor cells. Blood 116, 711–719. [PubMed: 20393131]

Kagey MH, Newman JJ, Bilodeau S, Zhan Y, Orlando DA, van Berkum NL, Ebmeier CC, Goossens J, Rahl PB, Levine SS, et al. (2010). Mediator and cohesin connect gene expression and chromatin architecture. Nature 467, 430–435. [PubMed: 20720539]

Kina T, Ikuta K, Takayama E, Wada K, Majumdar AS, Weissman IL, and Katsura Y (2000). The monoclonal antibody TER-119 recognizes a molecule associated with glycophorin A and specifically marks the late stages of murine erythroid lineage. Br J Haematol 109, 280–287. [PubMed: 10848813]

Kingsley PD, Greenfest-Allen E, Frame JM, Bushnell TP, Malik J, McGrath KE, Stoeckert CJ, and Palis J (2013). Ontogeny of erythroid gene expression. Blood 121, e5–e13. [PubMed: 23243273]

Kojic A, Cuadrado A, De Koninck M, Gimenez-Llorente D, Rodriguez-Corsino M, Gomez-Lopez G, Le Dily F, Marti-Renom MA, and Losada A (2018). Distinct roles of cohesin-SA1 and cohesin-SA2 in 3D chromosome organization. Nat Struct Mol Biol 25, 496–504. [PubMed: 29867216]

Kon A, Shih LY, Minamino M, Sanada M, Shiraishi Y, Nagata Y, Yoshida K, Okuno Y, Bando M, Nakato R, et al. (2013). Recurrent mutations in multiple components of the cohesin complex in myeloid neoplasms. Nat Genet 45, 1232–1237. [PubMed: 23955599]

Kuhn R, Schwenk F, Aguet M, and Rajewsky K (1995). Inducible gene targeting in mice. Science 269, 1427–1429. [PubMed: 7660125]

Lagasse E, and Weissman IL (1992). Mouse MRP8 and MRP14, two intracellular calcium-binding proteins associated with the development of the myeloid lineage. Blood 79, 1907–1915. [PubMed: 1373330]

Lajoie BR, Dekker J, and Kaplan N (2015). The Hitchhiker's guide to Hi-C analysis: practical guidelines. Methods 72, 65–75. [PubMed: 25448293]

Lakso M, Pichel JG, Gorman JR, Sauer B, Okamoto Y, Lee E, Alt FW, and Westphal H (1996). Efficient in vivo manipulation of mouse genomic sequences at the zygote stage. Proc Natl Acad Sci U S A 93, 5860–5865. [PubMed: 8650183]

Levine JH, Simonds EF, Bendall SC, Davis KL, Amir el AD, Tadmor MD, Litvin O, Fienberg HG, Jager A, Zunder ER, et al. (2015). Data-Driven Phenotypic Dissection of AML Reveals Progenitor-like Cells that Correlate with Prognosis. Cell 162, 184–197. [PubMed: 26095251]

Lieberman-Aiden E, van Berkum NL, Williams L, Imakaev M, Ragoczy T, Telling A, Amit I, Lajoie BR, Sabo PJ, Dorschner MO, et al. (2009). Comprehensive mapping of long-range interactions reveals folding principles of the human genome. Science 326, 289–293. [PubMed: 19815776]

Liu J, and Krantz ID (2009). Cornelia de Lange syndrome, cohesin, and beyond. Clin Genet 76, 303–314. [PubMed: 19793304]

Losada A, Hirano M, and Hirano T (1998). Identification of Xenopus SMC protein complexes required for sister chromatid cohesion. Genes Dev 12, 1986–1997. [PubMed: 9649503]

Love MI, Huber W, and Anders S (2014). Moderated estimation of fold change and dispersion for RNA-seq data with DESeq2. Genome Biol 15, 550. [PubMed: 25516281]

Mansson R, Zandi S, Anderson K, Martensson IL, Jacobsen SE, Bryder D, and Sigvardsson M (2008). B-lineage commitment prior to surface expression of B220 and CD19 on hematopoietic progenitor cells. Blood 112, 1048–1055. [PubMed: 18495958]

Mazumdar C, Shen Y, Xavy S, Zhao F, Reinisch A, Li R, Corces MR, Flynn RA, Buenrostro JD, Chan SM, et al. (2015). Leukemia-Associated Cohesin Mutants Dominantly Enforce Stem Cell

Programs and Impair Human Hematopoietic Progenitor Differentiation. Cell Stem Cell 17, 675–688. [PubMed: 26607380]

McKercher SR, Torbett BE, Anderson KL, Henkel GW, Vestal DJ, Baribault H, Klemsz M, Feeney AJ, Wu GE, Paige CJ, et al. (1996). Targeted disruption of the PU.1 gene results in multiple hematopoietic abnormalities. EMBO J 15, 5647–5658. [PubMed: 8896458]

Medina KL, Pongubala JM, Reddy KL, Lancki DW, Dekoter R, Kieslinger M, Grosschedl R, and Singh H (2004). Assembling a gene regulatory network for specification of the B cell fate. Dev Cell 7, 607–617. [PubMed: 15469848]

Mueller BU, Pabst T, Fos J, Petkovic V, Fey MF, Asou N, Buergi U, and Tenen DG (2006). ATRA resolves the differentiation block in t(15;17) acute myeloid leukemia by restoring PU.1 expression. Blood 107, 3330–3338. [PubMed: 16352814]

Mullenders J, Aranda-Orgilles B, Lhoumaud P, Keller M, Pae J, Wang K, Kayembe C, Rocha PP, Raviram R, Gong Y, et al. (2015). Cohesin loss alters adult hematopoietic stem cell homeostasis, leading to myeloproliferative neoplasms. J Exp Med 212, 1833–1850. [PubMed: 26438359]

Nora EP, Goloborodko A, Valton AL, Gibcus JH, Uebersohn A, Abdennur N, Dekker J, Mirny LA, and Bruneau BG (2017). Targeted Degradation of CTCF Decouples Local Insulation of Chromosome Domains from Genomic Compartmentalization. Cell 169, 930–944 e922. [PubMed: 28525758]

Nora EP, Lajoie BR, Schulz EG, Giorgetti L, Okamoto I, Servant N, Piolot T, van Berkum NL, Meisig J, Sedat J, et al. (2012). Spatial partitioning of the regulatory landscape of the X-inactivation centre. Nature 485, 381–385. [PubMed: 22495304]

Parelho V, Hadjur S, Spivakov M, Leleu M, Sauer S, Gregson HC, Jarmuz A, Canzonetta C, Webster Z, Nesterova T, et al. (2008). Cohesins functionally associate with CTCF on mammalian chromosome arms. Cell 132, 422–433. [PubMed: 18237772]

Pogosova-Agadjanyan EL, Kopecky KJ, Ostronoff F, Appelbaum FR, Godwin J, Lee H, List AF, May JJ, Oehler VG, Petersdorf S, et al. (2013). The prognostic significance of IRF8 transcripts in adult patients with acute myeloid leukemia. PLoS One 8, e70812. [PubMed: 23967110]

Pucella JN, Yen WF, Kim MV, van der Veeken J, Luo CT, Socci ND, Naito Y, Li MO, Iwai N, and Chaudhuri J (2015). miR-182 is largely dispensable for adaptive immunity: lack of correlation between expression and function. J Immunol 194, 2635–2642. [PubMed: 25672759]

Rao SS, Huntley MH, Durand NC, Stamenova EK, Bochkov ID, Robinson JT, Sanborn AL, Machol I, Omer AD, Lander ES, et al. (2014). A 3D map of the human genome at kilobase resolution reveals principles of chromatin looping. Cell 159, 1665–1680. [PubMed: 25497547]

Rao SSP, Huang SC, Glenn St Hilaire B, Engreitz JM, Perez EM, Kieffer-Kwon KR, Sanborn AL, Johnstone SE, Bascom GD, Bochkov ID, et al. (2017). Cohesin Loss Eliminates All Loop Domains. Cell 171, 305–320 e324. [PubMed: 28985562]

Reid S, Ritchie A, Boring L, Gosling J, Cooper S, Hangoc G, Charo IF, and Broxmeyer HE (1999). Enhanced myeloid progenitor cell cycling and apoptosis in mice lacking the chemokine receptor, CCR2. Blood 93, 1524–1533. [PubMed: 10029580]

Rubio ED, Reiss DJ, Welcsh PL, Disteche CM, Filippova GN, Baliga NS, Aebersold R, Ranish JA, and Krumm A (2008). CTCF physically links cohesin to chromatin. Proc Natl Acad Sci U S A 105, 8309–8314. [PubMed: 18550811]

Santambrogio F, and SpringerLink (Online service) Optimal Transport for Applied Mathematicians : Calculus of Variations, PDEs, and Modeling, 1st edn.

Schwarzer W, Abdennur N, Goloborodko A, Pekowska A, Fudenberg G, Loe-Mie Y, Fonseca NA, Huber W, C HH, Mirny L, et al. (2017). Two independent modes of chromatin organization revealed by cohesin removal. Nature 551, 51–56. [PubMed: 29094699]

Scott EW, Fisher RC, Olson MC, Kehrli EW, Simon MC, and Singh H (1997). PU.1 functions in a cell-autonomous manner to control the differentiation of multipotential lymphoid-myeloid progenitors. Immunity 6, 437–447. [PubMed: 9133423]

Seitan VC, Faure AJ, Zhan Y, McCord RP, Lajoie BR, Ing-Simmons E, Lenhard B, Giorgetti L, Heard E, Fisher AG, et al. (2013). Cohesin-based chromatin interactions enable regulated gene expression within preexisting architectural compartments. Genome Res 23, 2066–2077. [PubMed: 24002784]

Solomon DA, Kim T, Diaz-Martinez LA, Fair J, Elkahloun AG, Harris BT, Toretsky JA, Rosenberg SA, Shukla N, Ladanyi M, et al. (2011). Mutational inactivation of STAG2 causes aneuploidy in human cancer. Science 333, 1039–1043. [PubMed: 21852505]

Steidl U, Rosenbauer F, Verhaak RG, Gu X, Ebralidze A, Otu HH, Klippel S, Steidl C, Bruns I, Costa DB, et al. (2006). Essential role of Jun family transcription factors in PU.1 knockdown-induced leukemic stem cells. Nat Genet 38, 1269–1277. [PubMed: 17041602]

Su GH, Chen HM, Muthusamy N, Garrett-Sinha LA, Baunoch D, Tenen DG, and Simon MC (1997). Defective B cell receptor-mediated responses in mice lacking the Ets protein, Spi-B. EMBO J 16, 7118–7129. [PubMed: 9384589]

Sullivan C, Chen Y, Shan Y, Hu Y, Peng C, Zhang H, Kong L, and Li S (2011). Functional ramifications for the loss of P-selectin expression on hematopoietic and leukemic stem cells. PLoS One 6, e26246. [PubMed: 22039451]

Thota S, Viny AD, Makishima H, Spitzer B, Radivoyevitch T, Przychodzen B, Sekeres MA, Levine RL, and Maciejewski JP (2014). Genetic alterations of the cohesin complex genes in myeloid malignancies. Blood 124, 1790–1798. [PubMed: 25006131]

Toth A, Ciosk R, Uhlmann F, Galova M, Schleiffer A, and Nasmyth K (1999). Yeast cohesin complex requires a conserved protein, Eco1p(Ctf7), to establish cohesion between sister chromatids during DNA replication. Genes Dev 13, 320–333. [PubMed: 9990856]

Umemoto T, Yamato M, Shiratsuchi Y, Terasawa M, Yang J, Nishida K, Kobayashi Y, and Okano T. (2006). Expression of Integrin beta3 is correlated to the properties of quiescent hemopoietic stem cells possessing the side population phenotype. J Immunol 177, 7733–7739. [PubMed: 17114444]

van der Lelij P, Lieb S, Jude J, Wutz G, Santos CP, Falkenberg K, Schlattl A, Ban J, Schwentner R, Hoffmann T, et al. (2017). Synthetic lethality between the cohesin subunits STAG1 and STAG2 in diverse cancer contexts. Elife 6.

Vangala RK, Heiss-Neumann MS, Rangatia JS, Singh SM, Schoch C, Tenen DG, Hiddemann W, and Behre G (2003). The myeloid master regulator transcription factor PU.1 is inactivated by AML1-ETO in t(8;21) myeloid leukemia. Blood 101, 270–277. [PubMed: 12393465]

Viny AD, Ott CJ, Spitzer B, Rivas M, Meydan C, Papalexi E, Yelin D, Shank K, Reyes J, Chiu A, et al. (2015). Dose-dependent role of the cohesin complex in normal and malignant hematopoiesis. J Exp Med 212, 1819–1832. [PubMed: 26438361]

Wang H, Yan M, Sun J, Jain S, Yoshimi R, Abolfath SM, Ozato K, Coleman WG Jr., Ng AP, Metcalf D, et al. (2014). A reporter mouse reveals lineage-specific and heterogeneous expression of IRF8 during lymphoid and myeloid cell differentiation. J Immunol 193, 1766–1777. [PubMed: 25024380]

Wendt KS, Yoshida K, Itoh T, Bando M, Koch B, Schirghuber E, Tsutsumi S, Nagae G, Ishihara K, Mishiro T, et al. (2008). Cohesin mediates transcriptional insulation by CCCTC-binding factor. Nature 451, 796–801. [PubMed: 18235444]

Will B, Vogler TO, Narayanagari S, Bartholdy B, Todorova TI, da Silva Ferreira M, Chen J, Yu Y, Mayer J, Barreyro L, et al. (2015). Minimal PU.1 reduction induces a preleukemic state and promotes development of acute myeloid leukemia. Nat Med 21, 1172–1181. [PubMed: 26343801]

Yu G, Wang LG, and He QY (2015). ChIPseeker: an R/Bioconductor package for ChIP peak annotation, comparison and visualization. Bioinformatics 31, 2382–2383. [PubMed: 25765347]

Zandi S, Mansson R, Tsapogas P, Zetterblad J, Bryder D, and Sigvardsson M (2008). EBF1 is essential for B-lineage priming and establishment of a transcription factor network in common lymphoid progenitors. J Immunol 181, 3364–3372. [PubMed: 18714008]

Highlights

- Hematopoietic Stag2 loss enhances stem cell self-renewal and impairs differentiation
- Stag1 can maintain TAD boundary integrity in the absence of Stag2
- Stag2 is required for intra-TAD interactions at lineage genes (e.g. PU.1 targets)
- Stag2 target expression but not PU.1 overexpression restores B cell differentiation

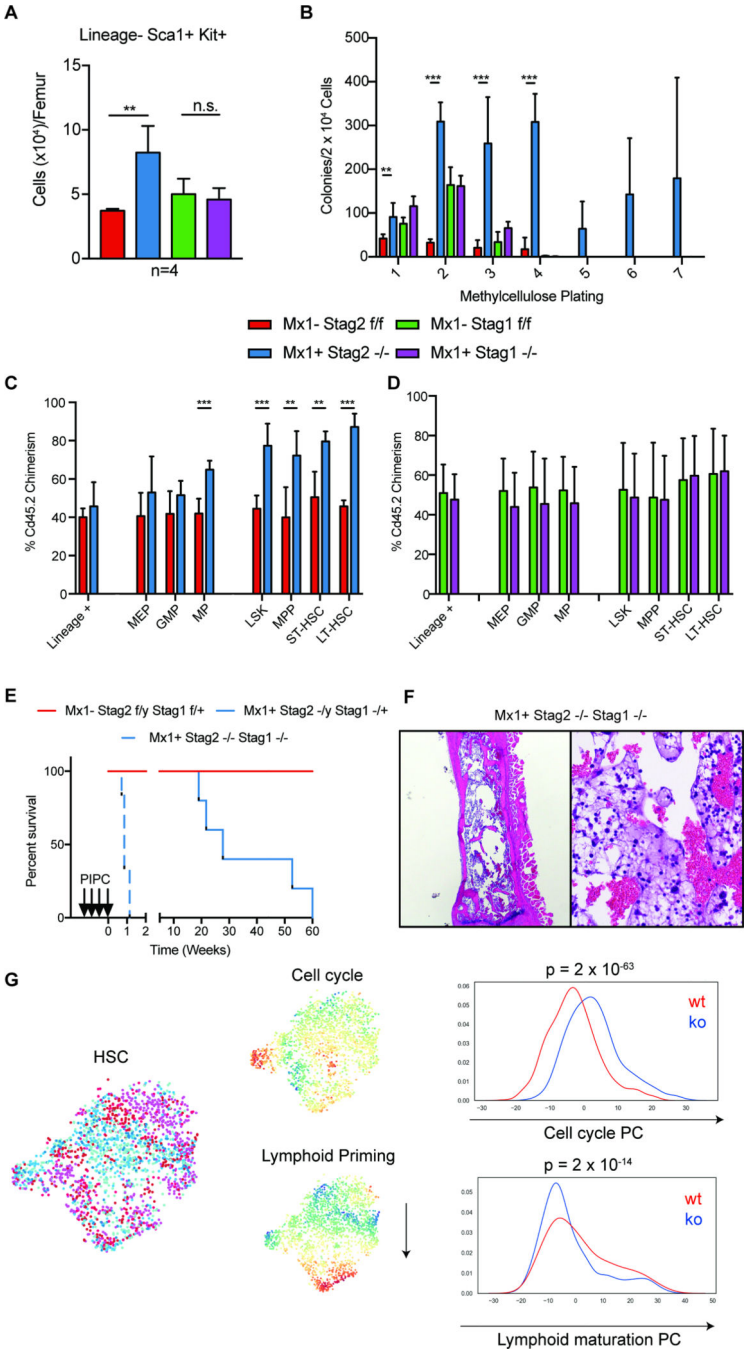

Fig 1. Hematopoietic specific loss of Stag2, but not Stag1, results in altered stem cell function.

A) Stag2 KO, but not Stag1 KO mice have increased LSK ($Lin^{-}Kit^{+}Sca1^{+}$) hematopoietic stem cells ($Log_2FC=2.2$; $p<0.01$) **B)** Whole bone marrow plated in cytokine-enriched methylcellulose. Stag2 KO marrow, but not WT and Stag1 KO, has increased self-renewal capacity and can serially replate (>7 platings). Competitive bone marrow transplantation of **C)** Stag2 WT (Red)/KO (Blue) or **D)** Stag1 WT (Green)/KO (Purple) bone marrow mixed 1:1 with Cd45.1 normal marrow. Stag2 KO shows increased chimerism in stem and progenitor populations in the bone marrow at 16 weeks. **E)** Kaplan-Meier curve shows

Stag2$^{-/y}$/Stag1$^{-/-}$ is lethal with a median survival of 0.7 weeks (p=0.01). Stag2$^{-/y}$/Stag1$^{-/+}$ has a lethal phenotype with a median survival of 27.7 weeks (p=0.05). **F)** Hematoxylin and eosin (H&E) staining of Stag2/Stag1 KO bone marrow reveals marked aplasia. **G**) Left: t-SNE projection of library-size normalized and log transformed data for inferred HSC subset (2025 cells). Each dot represents a single cell colored by genetic condition (Stag2 KO (shades of blue), Stag2 WT (shades of red). Middle: t-SNE projection colored by the second and third principal components most correlated with lymphoid priming and cell cycle, respectively. Right: Distribution of cells along lymphoid and cell cycle components; p-values for Mann-Whitney U test are shown.

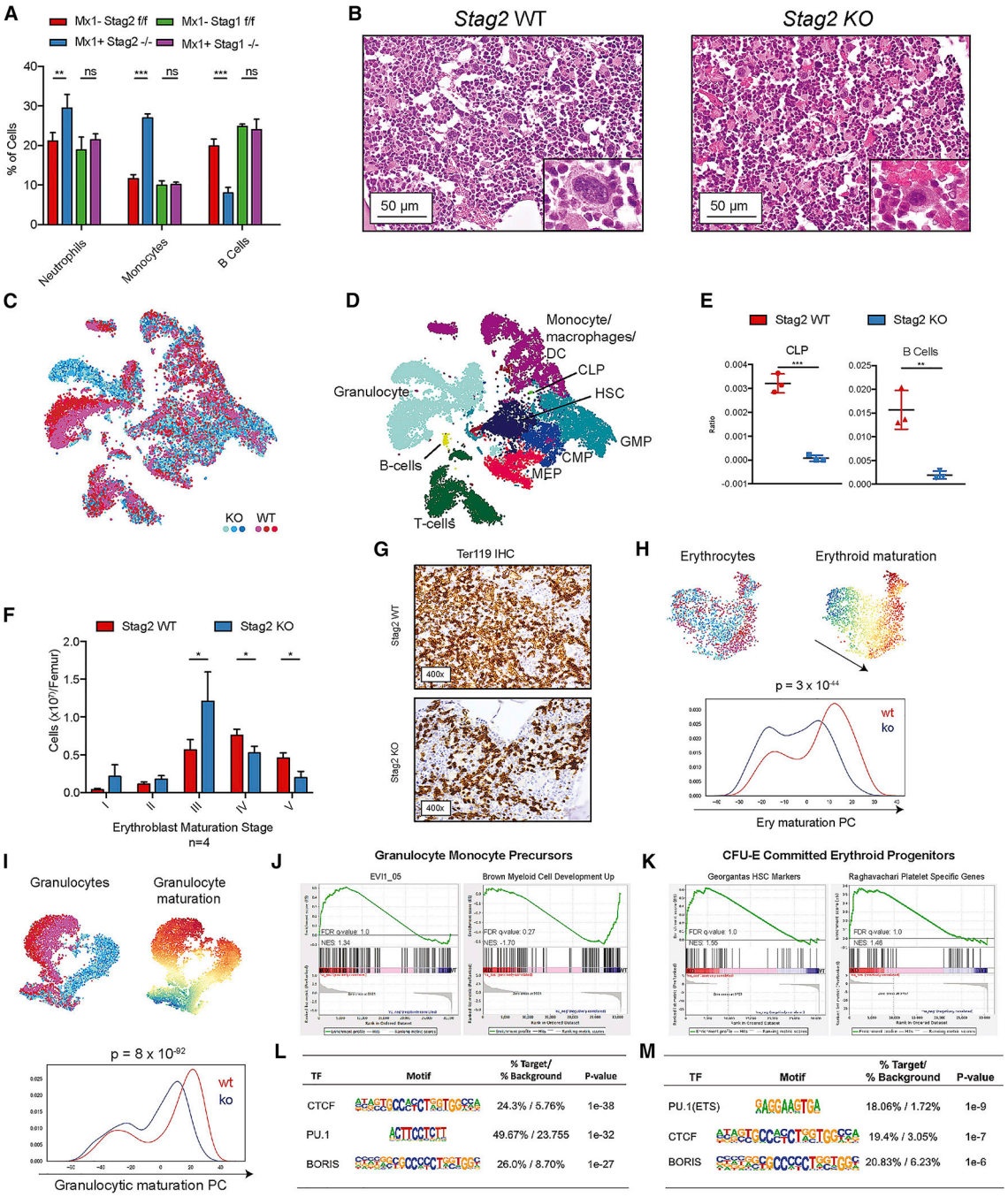

Fig 2. Stag2 alters transcriptional lineage commitment in stem and progenitor cells.

A) Peripheral blood with increase in Neutrophils ($Gr1^{+}Mac1^{hi}$), Monocytes ($Gr1^{+}Mac1^{lo}$), and decrease in B cells ($B220^{+}$) in Stag2 KO mice. No statistical differences were observed in Stag1 KO mice. **B)** Hematoxylin and eosin (H&E) staining of sternal bone marrow (400x) from Stag2 KO mice. Increased immature myeloid cells, nuclear-to-cytoplasmic dyssynchrony in erythropoiesis, and small, hypolobated megakaryocytes (Inset image, 1000x). **C)** Single cell RNA sequencing of Stag2 WT (n=3; shades of red) and Stag2 KO (n=3; shades of blue) Lin^{-} HSPC. (C) t-SNE projection of library-size normalized and log

transformed data for complete collection (24,153 cells). Each dot represents a single cell colored by genetic condition. **D**) t-SNE map colored by inferred cell type, as detailed in Figure S4. **E**) Frequency of CLPs (left) and B-cells (right) in Stag2 WT (red) and KO (blue) samples; asterisks indicate statistical significance (student's t test, **p<0.01, ***p<0.001) **F)** Flow cytometry of erythroblast stage in Stag2 WT and KO bone marrow reveals increased erythroblast stage III (p<0.05), reduction of mature erythroblast stage IV (p<0.02) and stage V (p<0.01). **G)** Immunohistochemical analysis of Stag2 WT and KO bone marrow reveals a marked reduction in Ter-119 expression in Stag2 KO. **H**) Top left: t-SNE projection of library-size normalized and log transformed data for inferred MEP subset (1787 cells). Each dot represents a single cell colored by genetic condition (Stag2 KO: shades of blue, Stag2 WT: shades of red). Top right: t-SNE projection colored by the second principal component most correlated with erythroid maturation. Bottom: Distribution of cells along erythroid maturation component. **I**) Top left: t-SNE projection of library-size normalized and log transformed data for inferred granulocytic subset (6316 cells). Each dot represents a single cell colored by genetic condition (Stag2 KO: blue, Stag2 WT: red). Top right: t-SNE projection colored by the first principal component most correlated with granulocyte maturation. Bottom: Distribution of cells along granulocyte maturation component. **J)** Gene-set enrichment analysis of GMP RNAseq shows increased expression of genes in the Evi1 gene set and decreased expression of myeloid development genes. **K)** CFU-E RNAseq shows enrichment for the Georgantas HSC markers gene set and retention of platelet specific genes. Integration of differentially expressed genes in **L)** GMP and **M)** CFU-E populations with ATAC-sequencing commonly have genes with CTCF/CTCFL (BORIS) motif signatures and PU.1 (ETS) motif signatures with decreased expression and decreased accessibility in both populations.

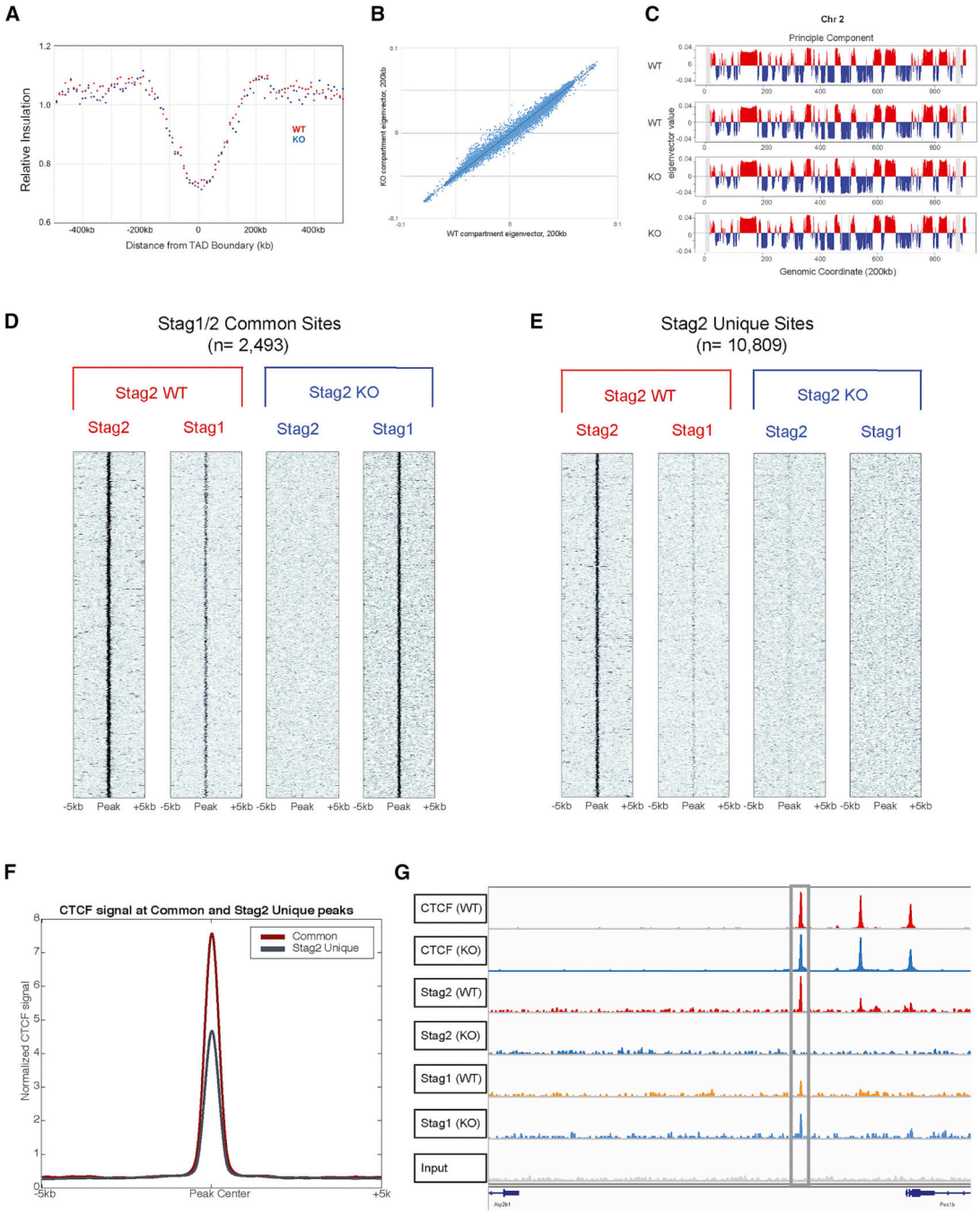

Fig 3. Stag2 and Stag1 possess shared and independent chromatin binding.

A) Insulation pileup plot from each dot shows the median of the interactions for each 200kb bins located 500kb upstream or downstream of a TAD border, normalized by the median interactions for WT and KO, respectively. **B)** Hi-C insulation scores were normalized by the median interactions for WT and KO, respectively. The diagonal bins were excluded for calculating the median. **C)** A/B compartments of chr2 for each biological replicate. The A compartments, positive PC1 signals, are highlighted in red, while the B compartments, negative PC1 signals, are highlighted in blue. **D)** Chromatin immunoprecipitation and

sequencing for Stag1 and Stag2 in Stag2 WT and KO HSPC show a discrete subset of the genome where Stag1 is able to bind Stag2 loci in its absence (common sites) and **E)** discrete loci where Stag1 is unable to bind in the absence of Stag2 (Stag2 unique sites). **F)** Enrichment of Stag1/2-common sites and Stag2-unique sites for CTCF shows strong enrichment in both sets. **G)** IGV track at TAD boundary as measured by Hi-C insulation on chromosome 10 showing CTCF occupancy as well as Stag2 in WT with Stag1 occupancy increased in Stag2 KO HSPC.

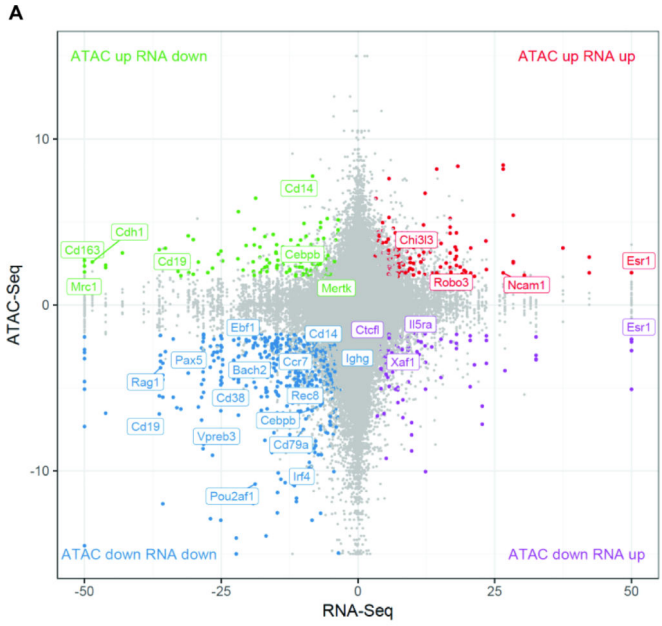

B

TF	Motif	% Target/ % Background	P-value
Gata	GAGATAAG	42.8% / 18.8%	1e-36
EBF	GGTCCCTGGGGG	15.6% / 5.68%	1e-16
E2A	GTGCCAGCTG	24.0% / 13.0%	1e-11

C

GeneID	ISC	Stag2 WT Peaks
Fgf1	-2.6	2
Pax5	-2.4	2
Lonrf2	-2.2	4
Gfra2	-2.2	2
Fcgr1	-2.1	2
Cpm	-2.0	2
Dtx1	-1.9	3
Ebf1	-1.9	2
0610040J01Rik	-1.9	2
Bach2	-1.4	6

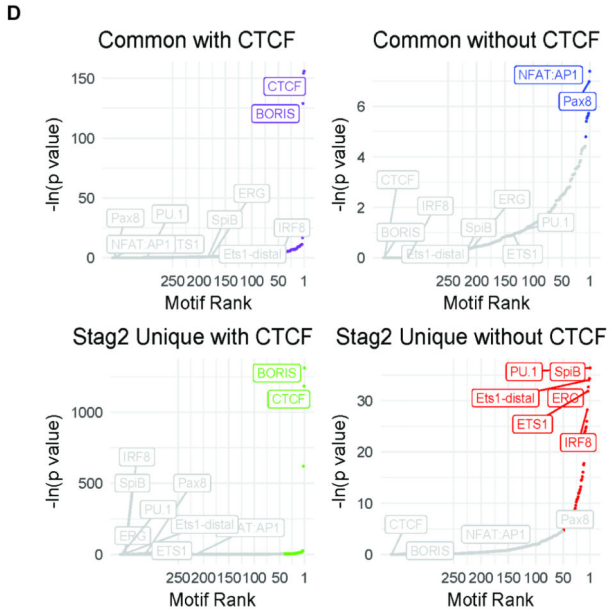

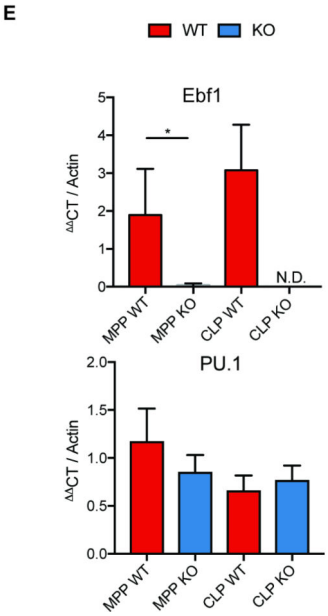

Fig 4. Stag2 loss decreases chromatin insulation and results in impaired transcriptional output.

A) Intersection of RNAseq and ATACseq in Lin$^-$ bone marrow plotted as −log10(pvalue) *sign of the Log_2 fold change of Stag2 KO compared to WT and each point representing a one ATAC peak. The majority of differentially expressed genes lose accessibility, including distinct B-cell regulators (e.g. *Ebf1, Pax5, Cd19*). **B)** HOMER motif analysis of genes in lower left quadrant of Figure 4A from intersection of RNAseq and ATACseq in Lin$^-$ bone marrow. Genes that are downregulated and lose accessibility are targets of Gata ($p=10^{-36}$), EBF ($p=10^{-16}$), and E2A ($p=10^{-11}$). **C)** Top 10 genes with greatest magnitude of ISC and number of WT Stag2 peaks in the gene. **D)** Motif analyses of common and Stag2-specific sites with and without CTCF show common enrichment for CTCF and CTCFL (BORIS).

Stag2-unique sites bind targets of key lineage priming factors PU.1, SpiB, ERG, ETS1, and IRF8, which Stag1 is unable to bind. **E)** Putative expressers of PU.1 and Ebf1 from Stag2 WT and KO bone marrow were sorted and *Ebf1* and *PU.1* expression was measured by RT-PCR in multipotent progenitors (MPP) and common lymphoid progenitors (CLP). Ebf1 expression was decreased in both populations (MPP p=0.04; CLP not detectable). PU.1 expression was not statistically different in either population (MPP p=0.13; CLP p=0.32).

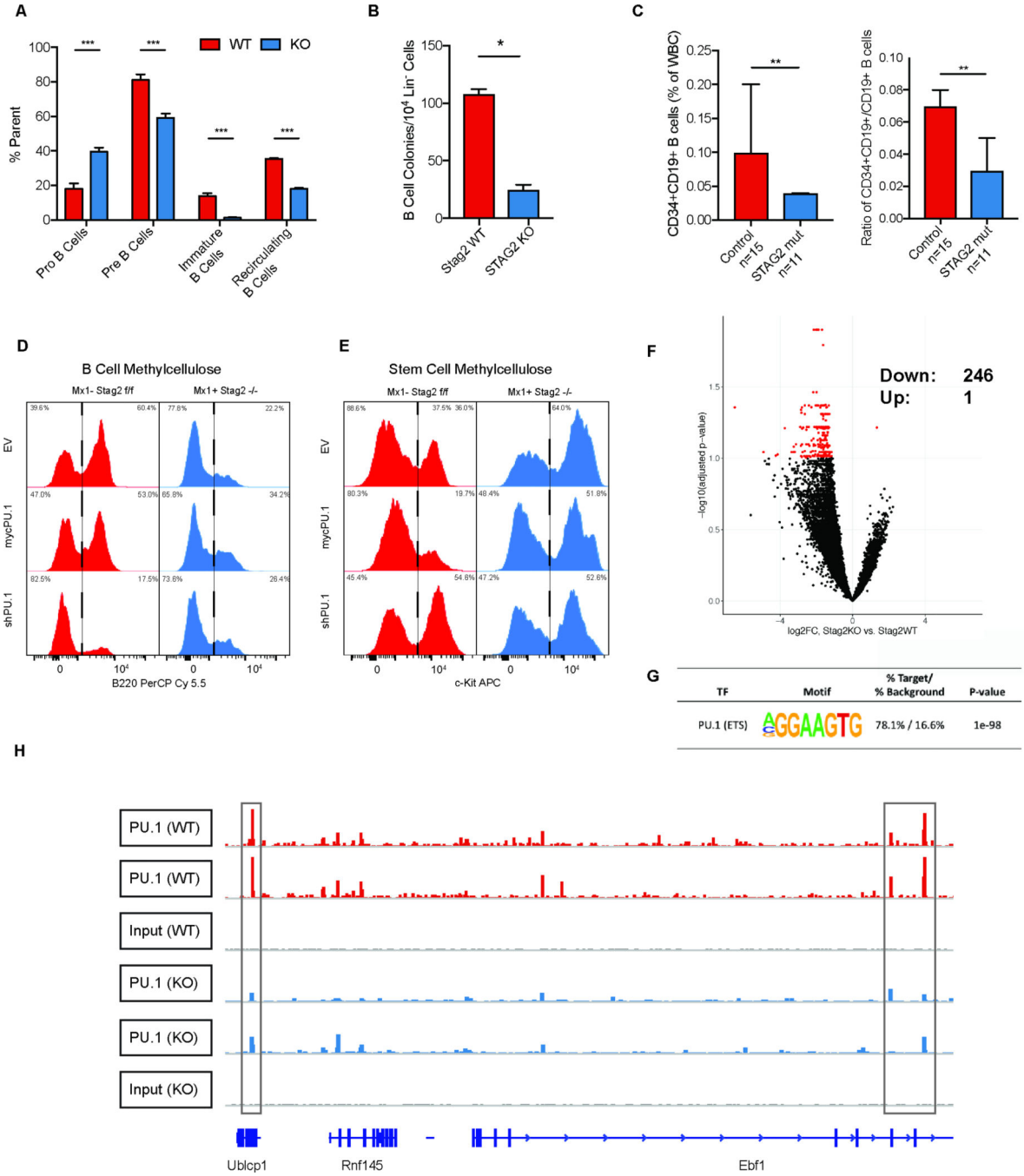

Fig 5. Altered Ebf1 chromatin structure results in a blockade of B cell development.

A) Enumeration of B lymphocyte maturation in Stag2 WT and KO mice. Bone marrow was analyzed using flow cytometry for pro- ($Cd43^{+}$) and pre- ($Cd43^{-}$) B-cells in parent gate $B220^{lo}IgM^{-}$ showing B-cell development block in the pro-B to pre-B transition ($p<0.003$). Immature ($B220^{lo}IgM^{+}$) and recirculating B cells ($B220^{hi}IgM^{+}$) were analyzed as a percentage of live singlets, which were both markedly reduced in Stag2 KO mice (asterisks indicate statistical significance (student's t test, **$p<0.01$, ***$p<0.001$). **B)** Methylcellulose colony enriched with IL-7, SCF, and FLT3-L shows reduction in the number of B cell

colonies in Stag2 KO bone marrow compared to WT ($p<0.003$). **C)** Enumeration of immature B cells (CD34+CD19+) and ratio compared to mature B cells (CD34-CD19+) show reduced immature B cells ($p<0.010$) and immature:mature ratio in STAG2 mutant MDS patients ($p<0.008$; n=11) compared to controls (n=15). **D-E)** Stag2 WT and KO HSPC were infected with lentivirus containing GFP-tagged empty vector, GFP-mycPU.1, or GFP-shPU.1; GFP^+ cells were plated in either B cell colony methylcellulose or stem cell methylcellulose. Cells were harvested after 7 days and analyzed by flow cytometry for (D) the B marker B220 or (E) stem cell marker cKit. **F)** Volcano plot for differentially PU.1-occupied loci by chromatin immunoprecipitation sequencing in HSPCs of Stag2 WT and Stag2 KO (data points in red indicate adjusted $p<0.1$). Loci with decreased in PU.1 occupancy in Stag2 KO to the left (n=246) and loci with increased in PU.1 occupancy in Stag2 KO to the right (n=1). **G)** HOMER analysis of 246 loci with decreased PU.1 binding shows enrichment for PU.1(ETS) motif ($p<10^{98}$). **H)** IGV track of the Ebf1 locus for Stag2 WT (n=2) and KO (n=2) shows decreased PU.1 binding at 3 loci (gray boxes).

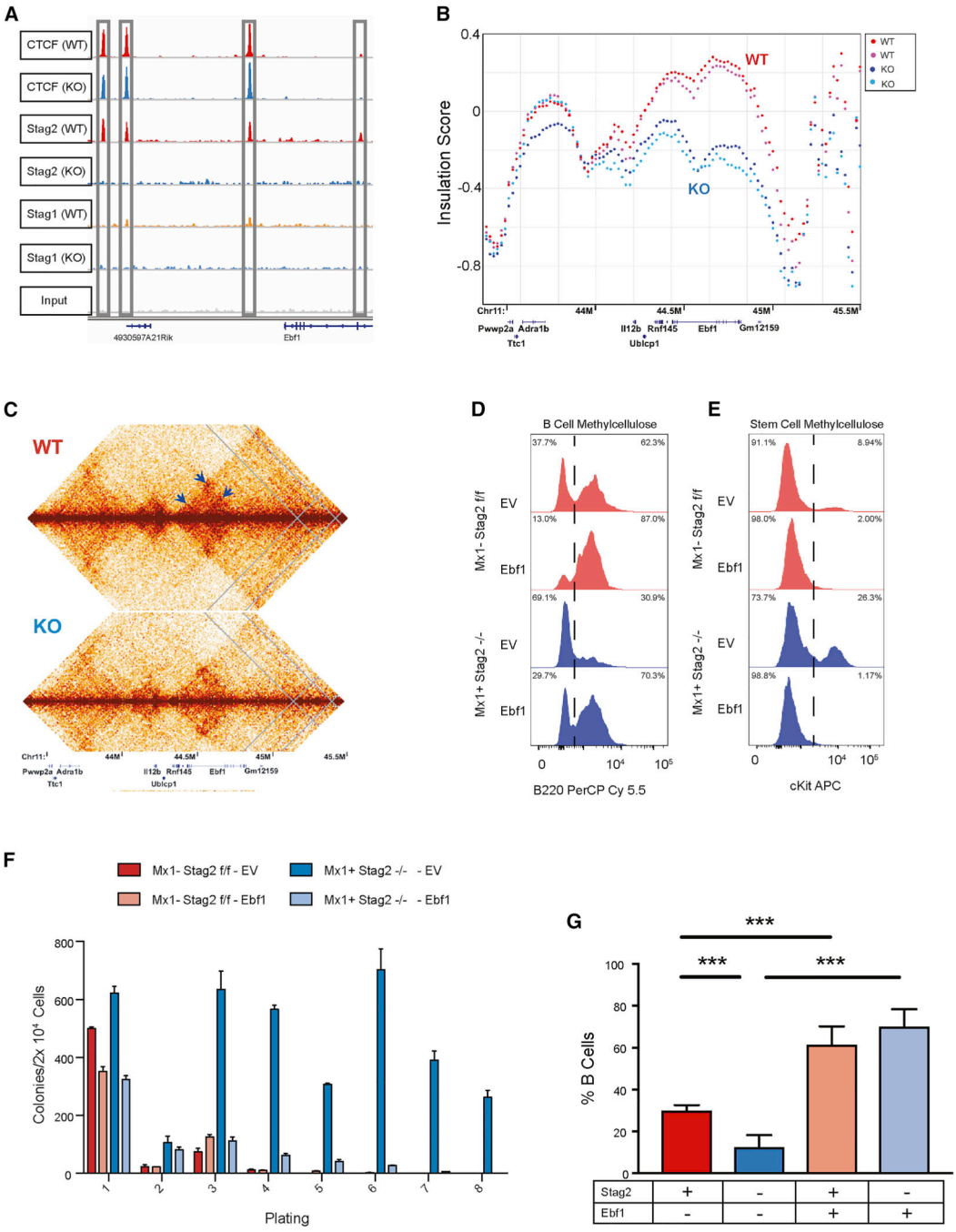

Fig 6. Induced Ebf1 expression rescues B cell development.

A) IGV track of the Ebf1 locus with Stag2 and Ctcf binding at 4 distinct sites lost in Stag2 KO and not bound by Stag1 either in WT or KO. **B)** ISC plotted across Ebf1 for Stag2 WT (n=2; shades of red) and KO (n=2; shades of blue) shows marked loss of insulation. **C)** Contact map of Ebf1 shows loss of cis-interaction at three loci (arrows). **D-E)** Lin^{-} Stag2 WT and KO marrow were infected with retrovirus containing GFP-tagged empty vector or GFP-pCMV-Ebf1. GFP^{+} cells were plated in either B-cell colony methylcellulose or stem cell methylcellulose. Cells were harvested after 7 days and analyzed by flow cytometry for

mature cell markers including (D) the B marker B220 or (E) stem cell markers including cKit. **F)** Cells plated in stem cell 10 methylcellulose were serially replated with exhaustion of Stag2 KO cell overexpressing Ebf1. **G)** GFP-tagged empty vector or GFP-pCMV-Ebf1 transduced Lin^- cells were injected into lethally irradiated CD45.1 recipient mice. Leukocyte populations from the parent gate (GFP^+, $Cd45.2^+$, $Cd45.1^-$) were analyzed by flow cytometry for percentage of mature B cells. Induced *Ebf1* expression restored B cell population frequency from the Stag2 KO HSPC ($p<0.001$). Asterisks 15 indicate statistical significance (student's t test, $^{**}p<0.01$, $^{***}p<0.001$)

KEY RESOURCES TABLE

REAGENT or RESOURCE	SOURCE	IDENTIFIER
Antibodies		
FITC anti-mouse CD11b	BioLegend	Cat#101205; RRID: AB_312788
PE anti-mouse CD11b	BioLegend	Cat#101207; RRID: AB_312790
APC/Cy7 anti-mouse CD11b	BioLegend	Cat#101225; RRID: AB_830641
PE anti-mouse Gr-1	BioLegend	Cat#108407; RRID: AB_313372
APC/Cy7 anti-mouse Gr-1	BioLegend	Cat#108423; RRID: AB_2137486
PE anti-mouse CD71	BioLegend	Cat#113807; RRID: AB_313568
APC anti-mouse Ter119	BioLegend	Cat#116211; RRID: AB_313712
APC/Cy7 anti-mouse Ter119	BioLegend	Cat#116223; RRID: AB_2137788
APC/Cy7 anti-mouse NK-1.1	BioLegend	Cat#108723; RRID: AB_830870
APC/Cy7 anti-mouse B220	BioLegend	Cat#103223; RRID: AB_313006
APC/Cy7 anti-mouse CD3	BioLegend	Cat#100221; RRID: AB_2057374
APC/Cy7 anti-mouse CD19	BioLegend	Cat#115529; RRID: AB_830706
APC/Cy7 anti-mouse CD4	BioLegend	Cat#100413; RRID: AB_312698
PE anti-mouse CD117/cKit	BioLegend	Cat#105807; RRID: AB_313216
APC anti-mouse CD117/cKit	BioLegend	Cat#105811; RRID: AB_313220
PE/Cy7 anti-mouse Sca-1	BioLegend	Cat#108113; RRID: AB_493597
APC anti-mouse Sca-1	BioLegend	Cat#108111; RRID: AB_313348
PE anti-mouse CD150	eBioscience	Cat#12-1502-82; RRID: AB_1548765
PerCP/Cy5.5 anti-mouse CD48	BioLegend	Cat#103421; RRID: AB_1575045
eFluor 450 anti-mouse CD16/32	eBioscience	Cat#48-0161-82; RRID: AB_1272191
eFluor 450 anti-mouse CD45.1	eBioscience	Cat#48-0453-82; RRID: AB_1272189
PE/Cy7 anti-mouse CD45.2	BioLegend	Cat#109829; RRID: AB_1186103
APC/Cy7 anti-mouse CD45.2	BioLegend	Cat#109823; RRID: AB_830788
PE anti-mouse CD34	BD Biosciences	Cat#551387 RRID: AB_394176
AlexaFluor 700 anti-mouse CD45.2	Biolegend	Cat#109822 RRID: AB_493731
PerCPCy5.5 anti-mouse CD16/32	Biolegend	Cat#101323 RRID: AB_1877268
PE Cy7 anti-mouse CD71	Biolegend	Cat# 113811 RRID:AB_2203383
APC anti-mouse CD44	Biolegend	Cat# 103011 RRID:AB_312962
PE anti-mouse CD41	Biolegend	Cat#133906 RRID:AB_2129745
FITC anti-mouse CD45.1	Biolegend	Cat#110706 RRID:AB_313495
cKIT (CD117) anti-mouse BV785	Biolegend	Cat#:105841 RRID:AB_2629799
PE anti-mouse IgD	Biolegend	Cat#: 405705 RRID:AB_315027
AlexaFluor700 anti-mouse CD19	Biolegend	Cat#: 302226 RRID:AB_493751
APC Cy7 anti-mouse CD43	Biolegend	Cat# 121220 RRID:AB_2194192
PerCP Cy5.5 anti-mouse CD45.2	Biolegend	Cat# 109828 RRID:AB_893350
PE Cy7 Anti-mouse CD45R/B220 antibody	BioLegend	Cat#103222 RRID: AB_313005
APC Anti-mouse Cd11b	BioLegend	Cat# 101212 RRID: AB_312795

REAGENT or RESOURCE	SOURCE	IDENTIFIER
PerCP Cy5.5 Anti-mouse CD3	BioLegend	Cat# 100218 RRID: AB_1595492
Brilliant Violet 421™ anti-mouse CD45.1 Antibody	BioLegend	Cat#110732 RRID: AB_2562563
Alexa 700 anti-mouse CD45.2	BioLegend	Cat# 109822 RRID: AB_493731
FITC anti-mouse CD45.1	BioLegend	Cat#110706 RRID: AB_313495
Alexa 700 anti-mouse CD45.2	BioLegend	Cat# 109822 RRID: AB_493731
APC Anti-mouse Cd11b	BioLegend	Cat# 101212 RRID: AB_312795
APC/Cy7 Anti-mouse CD117/cKIT	BioLegend	Cat# 105826 RRID: AB_1626278
Rabbit anti-SA2	Bethyl	Cat#A302-580A RRID: AB_2034860
Rabbit anti-SA1	Bethyl	Cat#A302-579A RRID: AB_2034857
Rabbit anti-SMC1a	Active Motif	Cat#61067 RRID: AB_2688006
Rabbit anti-PU.1	Cell Signaling	Cat#2266S RRID: AB_10692379
Rabbit anti-CTCF	Cell Signaling	Cat#3418S RRID: AB_2086791
Mouse anti-Actin	CalBiochem	Cat#JLA-20 RRID:AB_528068
Peroxidase Goat anti-Mouse IgM	CalBiochem	Cat#JA-1200
Goat anti-Rabbit IgG, HRP conjugate	Millipore	Cat#12-348 RRID:AB_390191
Bacterial and Virus Strains		
Biological Samples		
Patient samples	Memorial Sloan Kettering Cancer Center	Table S1
Chemicals, Peptides, and Recombinant Proteins		
Polyinosinic:polycytidylic acid	Amersham	Cat#27-4732-01
Bovine serum albumin	Fisher	Cat#BP1600-1
Phosphate Buffered Saline	MSKCC Media Core	N/A
RPMI medium	MSKCC Media Core	N/A
IMDM medium	MSKCC Media Core	N/A
Fetal bovine serum	MSKCC Media Core	N/A
Fetal calf serum	MSKCC Media Core	N/A
Penicillin-Streptomycin	Fisher	Cat#15140122
L-Glutamine	Thermofisher	Cat#21051040
Sodium Pyruvate	Thermofisher	Cat# 11360070
Colcemid	Gibco	Cat#15212012
MethoCult GF M3434	StemCell Technologies	Cat#03434
MethoCult M3630	StemCell Technologies	Cat#03630
Recombinant mouse GM-CSF	Peprotech	Cat#315-03
Recombinant mouse IL-3	Peprotech	Cat#213-13
Recombinant mouse SCF	Peprotech	Cat#250-03
Recombinant mouse IL-7	Biolegend	Cat# 577802
Recombinant mouse FLT3-L	Peprotech	Cat# 250-31
Dimethyl sulfoxide	Fisher	Cat#D128-500

REAGENT or RESOURCE	SOURCE	IDENTIFIER
16% Paraformaldehyde aqueous solution	Electron Microscopy Sciences	Cat#15710
DAPI	Sigma	Cat#D9542
RNase-free DNase set (50)	Qiagen	Cat#79254
TaqMan Master Mix (2X)	Thermofisher	Cat#4304437
Polybrene	American Bio	Cat#AB01643
HEPES buffer	Fisher	Cat#BP299
Retro-X concentrator	Takara	Cat# 631455
5M NaCl	Thermofisher	Cat#AM9760G
Tris-EDTA	Fisher	Cat#BP2473-500
0.5M EDTA, pH 8.0	Life Technologies	Cat#15575-020
SDS Solution, 20% Sodium Dodecyl Sulfate Solution	Fisher	Cat#BP1311-200
Sucrose	Sigma	Cat#84097-250G
1M MgCl2	Ambion(Thermo)	Cat#AM9530G
Tween 20	Sigma Aldrich	Cat#P7949-500mL
N,N-Dimethylformamide	Sigma Aldrich	Cat#D4551-250mL
Transposase,TAGMENT DNA Enzyme	Illumina	Cat# 15027865
Dynabeads Protein A	Invitrogen	Cat#10002D
Dynabeads Protein G	Invitrogen	Cat#10004D
Lithium Chloride	Acros Organics	Cat#413271000
TBS	Licor	Cat#927-50000
D1000 HS Buffer	Agilent	Cat#5190-6504
NP40	Fisher	Cat#FNN021
Deoxycholic Acid	Fisher	Cat#BP349-100
NaHCO3	Fisher	Cat#BP329-500
NaN3	USB	Cat#21610
Triton X-100	Sigma	Cat#0992-93-1
Igepal CA-630	Sigma	Cat#I8896
Halt protease inhibitors	Thermofisher	Cat#78429
Streptavidin beads (MyOne C1 beads)	Life Technologies	Cat#650.01
DpnII	NEB	Cat# R0543L
10X NEB 3.1 Buffer	NEB	Cat#B7203
Halt Protease Inhibitor Cocktail (100X)	Thermo	Cat#78429
Adenosine 5’-triphosphate magnesium salt from bacterial source (ATP) - 1G	Sigma	Cat#A9187-1G
Biotin-14-dATP	Invitrogen	Cat#19524-016
Biotin-14-dCTP	Invitrogen	Cat#19518-018
Proteinase K (Fungal)	Invitrogen	Cat#25530-031
DNA polymerase I, large (Klenow) fragment	NEB	Cat#M0210S
T4 DNA ligase 1U/ µl	Invitrogen	Cat#15224090
T4 DNA polymerase	NEB	Cat#M0203L

REAGENT or RESOURCE	SOURCE	IDENTIFIER
5X ligation buffer	Invitrogen	Cat#46300-018
T4 polynucleotide kinase	NEB	Cat#M0201
5X T4 DNA ligase buffer	Invitrogen	Cat#P/N y90001
Klenow fragment (3' → 5' exo$^-$)	NEB	Cat#M0212L
Agencourt AMPure XP	Beckman Coulter	Cat#A63881
Critical Commercial Assays		
Verso cDNA Synthesis Kit	Fisher	Cat#AB1453A
EasySep Mouse Hematopoietic Progenitor Cell Isolation Kit	STEMCELL Technologies	Cat# 19856
TruSeq Nano DNA kit	Illumina	Cat#20015965
Accel-NGS 2S Plus DNA Library Kit	Swift	Cat#21096
Accel NGS 2S MID Indexing Kit	Swift	Cat#27148
NEBNext® ChIP-Seq Library Prep Master Mix Set for Illumina	NEB	Cat# E6240L
DNA Clean and Concentrator - 5	Zymo	Cat# D4013
Deposited Data		
Gene Expression Omnibus (GEO:GSE134583)	N/A	RRID:SCR_005012
Experimental Models: Organisms/Strains		
Mouse: *Stag2$^{fl/fl}$*	The Jackson Laboratory	Cat#030902: RRID: IMSR_JAX: 030902
Mouse: *Stag1$^{fl/fl}$*	The Jackson Laboratory	Cat#030904: RRID: IMSR_JAX: 030904
Mouse: *Mx1-Cre*	The Jackson Laboratory	Cat#003556: RRID: IMSR_JAX: 003556
C57BL/6J	The Jackson Laboratory	Cat#000664: RRID: IMSR_JAX: 000664
B6.SJL-Ptprc^a/BoyAiTac	Taconic	Cat#4007: RRID: IMSR_TAC:4007
Oligonucleotides		
Stag2 NF 5′-CACTCATGCTGGCAAGTATTGTAC-3′	Invitrogen	N/A
Stag2-NR 5′-AACAGCCTGAGCAAAGAATCCAAAG-3′	Invitrogen	N/A
Stag2-3' 5′-TGTGTGCCTCTTTGAACAATGCCC-3′	Invitrogen	N/A
Stag1-CommonF 5′-GACTGGTATCTGACGGCTTATACC-3′	Invitrogen	N/A
Stag1-CommonR 5′-CACTGAGGACCAGGCATTGTAAGG-3′	Invitrogen	N/A
Stag1-FloxR 5′-TGAACTGATGGCGAGCTCAGACC-3′	Invitrogen	N/A
Mouse Stag2 RT-PCR For 5'-TGCTATGCAGTCGGTGGTAG-3'	Invitrogen	N/A
Mouse Stag2 RT-PCR Rev 5'-AGGACCAGCCATGGTAAGTG-3'	Invitrogen	N/A

REAGENT or RESOURCE	SOURCE	IDENTIFIER
Mouse Stag1 RT-PCR For 5'-GAGTCCTGATTCGACAGTGTCA-3'	Invitrogen	N/A
Mouse Stag1 RT-PCR Rev 5'-AGGGTACTTGTATGCCTAAAAGC-3'	Invitrogen	N/A
Mouse Actin RT-PCR For 5'-GGCTGTATTCCCCTCCATCG-3'	Invitrogen	N/A
Mouse Actin RT-PCR Rev 5'-CCAGTTGGTAACAATGCCATGT-3'	Invitrogen	N/A
Taqman Spi1 (PU.1) Probe	Thermofisher	Mm00488140_m1
Taqman Ebf1 Probe	Thermofisher	Mm00432948_m1
Taqman Actin Probe	Thermofisher	Mm02619580_g1
Recombinant DNA		
pMSCV-IRES-GFP	Mulligan Lab	N/A
pMSCV-IRES-GFP-Ebf1	Mulligan Lab	N/A
pCAD-IRES-GFP	Will et al., 2015	N/A
pCAD-IRES-GFP-PU1	Will et al., 2015	N/A
pRRLsin-PGK-eGFP-WPRE	Will et al., 2015	N/A
pRRLsin-PGK-eGFP-WPRE-PU1	Will et al., 2015	N/A
EcoPack plasmids	Will et al., 2015	N/A
pRRLsin-PGK-eGFP-WPRE	Will et al., 2015	N/A
psPAX2	Will et al., 2015	N/A
pMD2.G	Will et al., 2015	N/A
Software and Algorithms		
Prism 6	GraphPad	https://www.graphpad.com
FlowJo V9.9.6	Tree Star	https://www.flowjo.com/
Other		